Influence of Dopants and Electrical Fields on Grain Growth in Alumina

Noy Fabri

Influence of Dopants and Electrical Fields on Grain Growth in Alumina

Research Thesis

In Partial Fulfillment of the
Requirements for the Degree of
Master of Science in Materials Engineering

Noy Fabri

Submitted to the Senate of the Technion-Israel Institute of Technology

Cheshvan 5782 Haifa November 2022

The research thesis was done under the supervision of **Prof. W.D. Kaplan** in the Department of Materials Science & Engineering.

Acknowledgements

I wish to thank the Technion for partial financial support of this study. This research was partially supported by the Israel Science Foundation (Grant No.1779/18) and by Bitossi Industries.

The author of this thesis states that the research, including the collection, processing and presentation of data, addressing and comparing to previous research, etc., was done entirely in an honest way, as expected from scientific research that is conducted according to the ethical standards of the academic world. Also, reporting the research and its results in this thesis was done in an honest and complete manner, according to the same standards.

Table of Contents

Acknowledgements I

Table of Contents I

List of Figures IV

List of Tables IX

Abstract 1

List of Symbols and Abbreviations 2

1. Literature Survey 5

1.1 Sintering 5

1.1.1 Solid State Sintering 6

1.1.2 Liquid Phase Sintering (LPS) 6

1.1.3 Field Induced Sintering 7

1.2 Grain Boundary Mobility and Grain Growth 9

1.2.1 Grain Growth 9

1.2.2 Grain Growth Mechanism 9

1.2.3 Grain Boundary Mobility Measurements 11

1.2.4 Solute Drag/Acceleration 12

1.2.5 Zener Drag 13

1.2.6 Liquid Phase Effect 16

1.3 Alumina 17

1.3.1 The Influence of Dopants on Alumina Grain Boundary Mobility 18

2. Research Goals 20

3. Experimental Methods 21

3.1 Sample Preparation 21

3.1.1 Undoped Alumina 21

3.1.2 Mg Doped Alumina 22

3.1.3 Laboratory RTP Alumina 22
3.1.4 Alumina Co-doped with Ca and Si 22
3.1.5 Commercial RTP Alumina 99.5% 24
3.1.6 Commercial RTP Alumina 98% 24
3.2 Thermal Treatments 25
3.3 Characterization 26
3.3.1 Density 26
3.3.2 Wavelength Dispersive Spectroscopy 26
3.3.3 X-ray Diffraction 27
3.3.4 Scanning and Scanning/Transmission Electron Microscopy 28
3.3.5 Grain Size Analysis 28
3.3.6 Specimen Preparation for Characterization 28
4. Results 30
4.1 Phase Analysis 30
4.1.1 Undoped Alumina 30
4.1.2 Mg Doped Alumina 31
4.1.3 RTP Alumina 32
4.1.4 Commercial RTP Alumina 99.5% 32
4.1.5 Commercial RTP Alumina 98% 38
4.2 Grain Boundary mobility of alumina at 1600°C 41
4.2.1 Microstructure 41
4.2.2 Grain Growth: Composition Effect 43
4.2.3 Grain Growth: Furnace Effect 44
4.2.4 Grain Boundary Mobility 45
4.3 Glass Exudation from Grain Boundaries 47
4.4 Wear Rate 50
5. Discussion 54

5.1 The Influence of a Field on Grain Boundary Mobility 54
5.2 The influence of carbon on Grain Boundary Mobility 56
5.3 The Influence of Liquid Phase on Grain Boundary Mobility 57
5.3.1 Undoped Sample 57
5.3.2 Samples with a Liquid Phase 59
5.3.3 Glass Coverage 62
5.3.4 Wear rate 68
5.4 Exudation 68
6. Summary and Conclusions 71
7. Recommendations for Future Work 72
8. References 73

List of Figures

Figure 1: Schematic illustration of densification and grain growth during sintering, where the driving force for sintering is the reduction of the surface component of free energy. 6

Figure 2: Schematic drawing of the microstructure changes during LPS.. 7

Figure 3: Schematic illustration of the SPS configuration 8

Figure 4: Schematic drawing of the induction sintering configuration.....9

Figure 5: Schematic drawing of grain boundary migration from a concave to a convex grain..10

Figure 6: TLK model for describing atom motion on surfaces.....10

Figure 7: Schematic representation of solute drag mechanism in crystalline ceramics. (a) is a symmetrical distribution of the dopant in the region of a stationary grain boundary, (b) is an asymmetric distribution produced by the moving boundary, and (c) is breakaway of the boundary from the dopant leaving a solute cloud behind. 12

Figure 8: Driving force velocity behavior for (a) intrinsic migration (b) solute drag only and (c) total force velocity.....13

Figure 9: Pore boundary interaction as a function of grain and pore size, assuming pores migrate by surface diffusion.....15

Figure 10: Schematic drawing of the hexagonal (a) and rhombohedral (b) unit cells of α-alumina. The blue spheres represent aluminum cations, and the red spheres represent oxygen anions 17

Figure 11: a) SEM micrograph of the microstructure of alumina doped with 100 ppm of SiO_2 and 50 ppm of CaO and sintered at 1620°C for 12 h; b) TEM micrograph of a faceted grain boundary. 19

Figure 12: Photograph of the Buchner funnel used for vacuum filtration of the alumina slip. 21

Figure 13: BSE SEM micrograph of a cross-sectioned infiltrated alumina sample containing secondary phase particles. 24

Figure 14: SE SEM micrograph of the microstructure of undoped alumina sintered for 2 h…31

Figure 15: SE SEM micrograph of the microstructure of Mg doped alumina sintered for 2 h. 31

Figure 16: SE SEM micrograph of the microstructure of RTP alumina sample sintered for 2 h. 32

Figure 17: XRD pattern of commercial RTP alumina sample containing 0.5% of glass, presenting only alumina reflections. Reflections from a second phase were not detected. 33

Figure 18: HAADF STEM micrograph showing second phase at triple junctions and some of the grain boundaries. 34

Figure 19: a) HAADF STEM micrograph of a selected area for EDS at a grain boundary. b) HAADF STEM micrograph combined with elemental EDS map. c-h) individual EDS maps at the grain boundary showing Na, O, Al, Mg, Si, and Ca.....35

Figure 20: EDS spectrum acquired from the grain boundary indicated as areas 1 and 2 in Figure 19 36

Figure 21: a) HAADF STEM micrograph of selected areas for EDS at a triple junction. b) HAADF STEM micrograph combined with elemental EDS map. c-h) individual EDS maps at a triple junction for Na, O, Al, Mg, Si, and Ca.....36

Figure 22: EDS spectrum from a triple junction in areas 1 and 2 in Figure 21. 37

Figure 23- a) HRTEM micrograph of commercial RTP alumina sample edge, showing a crystalline alumina grain below an apparently amorphous area. b) Electron diffraction pattern acquired from the apparently amorphous area in a, showed diffuse rings, confirming it is amorphous. 37

Figure 24: SE SEM micrograph of the microstructure of commercial RTP alumina sample sintered for 4 h. 38

Figure 25: XRD pattern of commercial alumina sample containing 2% of glass, presenting only alumina reflections. Reflections from a second phase were not detected. 39

Figure 26: BSE SEM micrograph showing a second phase (marked with arrow) in the commercial 98% alumina sample annealed for a) 1 min and b) 10 h in an air furnace, polished without thermal etching. 39

Figure 27: SE SEM micrograph of the microstructure of a commercial 98% alumina sample sintered for 2 h. 40

Figure 28: SE SEM micrograph of the microstructure evolution of the commercial 98% alumina samples, annealed in an air furnace for: a) 1 h, b) 3 h, and c) 10 h. 40

Figure 29: SE SEM micrographs of the microstructure of: a) undoped alumina; b) Mg-doped alumina; c) RTP alumina; d) commercial RTP alumina annealed for 1 h at 1600°C in 1- air furnace; 2- graphite furnace; or 3- field assisted furnace. 42

Figure 30: Grain growth kinetics of undoped, Mg doped, RTP and commercial RTP alumina samples annealed for various times at 1600°C in a) an air furnace, b) a graphite furnace and c) a field assisted furnace. 43

Figure 31: Grain growth kinetics of commercial RTP alumina 98% annealed for various times at 1600°C in an air furnace, exhibiting two growth regimes: initial (orange) and exaggerated (blue). 44

Figure 32: Grain growth kinetics of a) undoped, b) Mg doped, c) RTP and d) commercial RTP alumina samples, annealed at the different furnaces for various times at 1600°C. 45

Figure 33: Effective mobilities presented in a graphical form (logarithmic scale).....47

Figure 34: a) SE SEM micrograph of commercial RTP alumina sample thermally etched in an air furnace showing exuded glass at the grain boundaries. b) Thermally etched in a graphite furnace under flowing He showing no exuded phase at the grain boundaries. c) Sample b that underwent another thermal etch in an air furnace showing exuded glass at the grain boundaries. d) Thermally etched in a sapphire tube furnace under Ar showing exuded glass at the grain boundaries. 48

Figure 35: a) SE SEM micrograph of a sample (sectioned using the FIB) of a grain boundary cross-section in a sample annealed in air showing a glassy phase exuded from the boundary and partially wetting the grains. b) FIB micrograph of a grain boundary cross-section in a sample annealed in a graphite furnace under He. 49

Figure 36: SE SEM micrograph of a soda-lime drop on a sapphire c-plane annealed for 2 h at 1250°C in: a) an air furnace, b) a graphite furnace (same scale bar for a and b). ..49

Figure 37: SE SEM micrograph of a sample (sectioned using the FIB) of (a) a drop cross-sectioned after annealing in an air furnace. The contact angle between the glass and the sapphire is marked in red. b) A collapsed drop of soda-lime glass on a sapphire

c-plane surface annealed in a graphite furnace, where the void is marked with an arrow (same scale bar for a and b). 50

Figure 38: Wear rate of the different samples: laboratory RTP (blue), commercial RTP 99.5% (orange), commercial RTP 98% (purple) and commercial 90% (grey). 51

Figure 39: SE SEM micrographs of the wear surface for a) laboratory RTP alumina, b) commercial RTP 99.5% alumina and c) commercial RTP 98% alumina. Areas of tribofilm (marked in arrows) formed during cutting is shown in all samples. The micrographs show the bottom of a cutting groove, where abrasive wear by cutting took place (same scale bar for a, b and c).....52

Figure 40: SE SEM micrograph of the wear surface for 90% alumina sample. The micrographs show the bottom of a cutting groove, where abrasive wear by cutting took place. Visible pores with a diameter of the order of the diameter of abnormal grains are present at the cut grove and also fractured surface (marked in red arrows).....53

Figure 41: Effective grain boundary mobility for undoped alumina annealed in an air furnace, compared to effective mobility values from the literature. 58

Figure 42: k ratio of commercial RTP 99.5% and 98% alumina compared with k ratio values from the literature for samples with varying amount of glass. Samples that contained only glass are marked in black, samples with additional doping of MgO marked in red. The commercial RTP samples in this current study contain Mg above solubility limit. 60

Figure 43: Glass coverage calculated for commercial RTP 99.5% alumina for three thickness layers: 1µm, 50 nm and 2 nm. 62

Figure 44:Glass coverage calculated for commercial RTP 98% alumina for three thickness layers: 1µm, 50nm and 2 nm. 63

Figure 45: (a) Large-scale cross-sectional TEM view of a 3° basal tilt boundary viewed along the common a-axis of rotation. On this scale, the boundary is seen to consist of narrow, planar segments (designated as “dewetted”) separated by interfacial glass pockets elongated along the boundary. (b) Selected area electron diffraction pattern confirming the 3° basal tilt misorientation. (c) Representative EDS spectrum from “dewetted” portion of boundary showing the presence of Si and Ca adsorbates at the boundary 65

Figure 46: The influence of composition on the mobility of a single grain boundary. 66

Figure 47: The influence of composition on the mobility in a polycrystalline material (with many 67

Figure 48: illustration of grain boundary with a grooved surface, showing the dihedral angles θ, ϕ and the interface energies γint.....69

List of Tables

Table 1: List of thermal treatments conducted for each of the samples studied in this research. 26

Table 2: EDS measurements of the second phase (Figure 26a, marked in arrow) overlapping with alumina grain, showing the elemental distribution. 39

Table 3: Summary of the dopant/impurity concentration of the samples. 40

Table 4: Summary of all measured grain boundary effective mobility values. 46

Table 5: Summary of samples for wear rate experiment 50

Abstract

It is well known that dopants and/or impurities can cause significant changes to the grain boundary mobility of materials. This can occur by equilibrium (Gibbsian) segregation of solutes to grain boundaries, driven by a reduction in grain boundary energy, and resulting in solute-drag or solute-acceleration. Alternatively, above the solubility limit, dopants and/or impurities can result in precipitation of secondary phases, which can reduce grain boundary mobility by Zener drag. Above the solubility limit of common alumina impurities, a (partially) wetting phase can form at grain boundaries that acts as a grain boundary mobility reducing/accelerating mechanism. Several studies showed that sintering in the presence of a liquid phase (liquid phase sintering) can result in a dense microstructure, although the influence of the liquid phase on grain growth is not clear.

External electromagnetic fields are also known to influence the rate of sintering and microstructural evolution. A full understanding of how fields influence processing kinetics of alumina has yet to be achieved.

In this study, the influence of key dopants below and above the solubility limit, some forming a liquid phase, on grain growth of dense alumina was studied. The influence of different atmospheres (air, CO/CO_2 and field-assisted) on the effective grain boundary mobility was studied. Over one order of magnitude increase in effective mobility was observed for all samples annealed under a field, regardless of the dopant concentration, meaning there is an increase in the effective grain boundary mobility in the presence of an electric field, even in the presence of Mg which is a known solute-drag dopant. The addition of a liquid phase at grain boundaries decreased the effective mobility of grain boundaries compared to undoped samples.
.

List of Symbols and Abbreviations

E_a	Activation energy
AC	Alternating current
Z	Atomic number
$\bar{G}_t^2$	Average squared grain size
$\overline{G_{t=0}}^2$	Average squared grain size at t=0
I_{bgd}	Background intensity
BSE	Backscattered electrons
C_∞	Bulk solute concentration
$°C$	Celsius degrees
CIP	Cold isostatic presure
C_{std}	Concentration of element of interest in the standard
$[X]$	Concentration of element X
C	Concentration of the element of interest
$\theta_{Al_2O_3-glass}$	Contact angle between the exuded glass and alumina
g_{ZAF}	Correction factor for atomic number, absorption, and fluorescence
E_c	Critical excitation energy
G_c	Critical grain radius
ρ	Density
δr	Difference between the radius of the solvent and solute
D	Diffusion coefficient
D_o	Diffusion constant
ψ	Dihedral angle
DC	Direct current
β	Drift velocity
F_b	Driving force per unit area for boundary motion
D	Dry weight
EELS	Electron energy loss spectroscopy
EDS	Energy dispersive spectroscopy
FIB	Focused ion beam

R	Gas constant
α	Geometrical shape factor
n	Geometric factor
V_{GB}	Grain boundary velocity
γ_{GB}	Grain boundary energy
G	Grain size
γ_{GB}	Grain boundary energy
HAADF	High angle annular dark field
HPA	High purity alumina
HRTEM	High resolution transmission electron microscopy
h	Hour
E_0	Incident electron energy
K	Interface reaction-rate constant
I	X-rays intensity
F_0	Intrinsic drag
$C_{\mathrm{lim},0.95}$	Limit of detection (at a confidence larger than 95%)
τ	Measurement time
M	Molar mass
m	Number of measurements
P_{O_2}	Oxygen partial pressure
N_Z	Particle or pore density at the grain boundary
F_Z	Pining force
P	Pressure
r	Radius
k	Ratio of intensity of characteristic X-ray radiation measured from the sample to that measured from the standard
F_r	Retarding force
RTP	Ready to press
W	Saturated weight
SEM	Scanning electron microscopy
STEM	Scanning transmission electron microscopy

SE	Secondary electrons
SAD	Selected area diffraction
F_s	Solute drag
α_s	Solute drag force per unit velocity per unit solute concentration
S*	Solubility at the surface of the solid grain
SPS	Spark plasma sintering
$\Delta\mu^{\Theta}_{\lvert V_O \rvert}$	Standard chemical potential for oxygen vacancy
γ_s	Surface or interface energy
S	Suspended weight
T	Temperature
TLK	Terrace-Ledge-Kink model
x	Thickness
δ	Thickness of the liquid layer
t	Time
A	Total interface area
TEM	Transmission electron microscopy
WDS	Wavelength dispersive X-ray spectroscopy
XRD	X-ray diffraction
θ	X-ray take-off angle

1. Literature Survey

1.1 Sintering

Ceramics have high melting temperatures which make them difficult to melt and cast. In order to process a ceramic material thermal energy, of the order of 0.5-0.8T_m, is applied to a green body which is made of compacted powder. This provides enough atomic mobility for the material to densify. The driving force for sintering is the reduction of surface excess energy [1]:

$$\Delta(\gamma A) = \Delta\gamma A + \gamma\Delta A \quad (1)$$

where γ is the surface/interface energy, A is the total surface/interface area and γA is the total surface/interface energy.

During sintering two competing phenomena occur (Figure 1):

1. Densification, which is the desired outcome, where the free surface of the particles is replaced by grain boundary area that has lower energy, hence $\Delta\gamma$ is reduced.
2. Grain growth (coarsening), where the specific excess surface energy itself is not reduced but the total grain boundary area ΔA is, hence the total energy in the system γA will be lower.

Densification results in the elimination of pores and coarsening results in the growth of the grains. Although grain growth is insignificant at the beginning of the sintering process, it becomes substantial with densification and has a considerable influence on the final density and the resulting microstructure.

Sintering remains among the most viable methods of fabricating novel ceramics, enabling controlled density and microstructure, which translates to a variety of controlled mechanical, optical and electrical properties. Yet, further understanding of the mechanics of densification and grain growth during sintering will allow better engineering control.

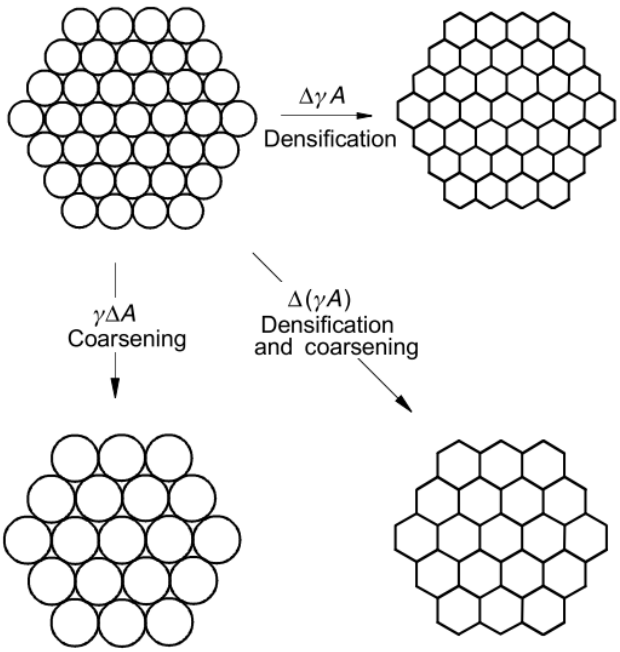

Figure 1: Schematic illustration of densification and grain growth during sintering, where the driving force for sintering is the reduction of the surface component of free energy [1].

1.1.1 Solid State Sintering

During solid state sintering, mass transport occurs in several ways including surface diffusion, grain boundary diffusion, volume diffusion and vapor transport (from the solid-vapor interface to around the neck) [2]. Transfer of matter from the particle volume or from the grain boundary between particles causes shrinkage and pore elimination. Coble identified three stages of solid-state sintering [3]. In the first stage necks between adjacent particles start to form, hence grain boundaries start to form, and grain growth initiates. During the intermediate stage the neck area grows, and pores start to form arrays of cylindrical interconnected channels and the cylindrical pores simply shrink via diffusion in grain boundaries or volume diffusion. The final stage ends after pores are separated from one another, the grain boundary area is reduced by grain growth and full density is achieved only if pores move together with the grain boundaries and don't disconnect to be entrapped (occluded) inside the grains.

1.1.2 Liquid Phase Sintering (LPS)

During liquid state sintering a secondary molten liquid phase is present between the solid grains. This can result from dopants and/or impurities present in the ceramic powders which are rejected to the grain boundaries during sintering and accumulate as grains grow [4]. Provided that the liquid phase wets the grains it induces capillary forces that pull the grains together

(Figure 2). Furthermore, because of solute diffusion in the liquid, the liquid is believed to improve transport rates responsible for grain coarsening and densification [5,6].

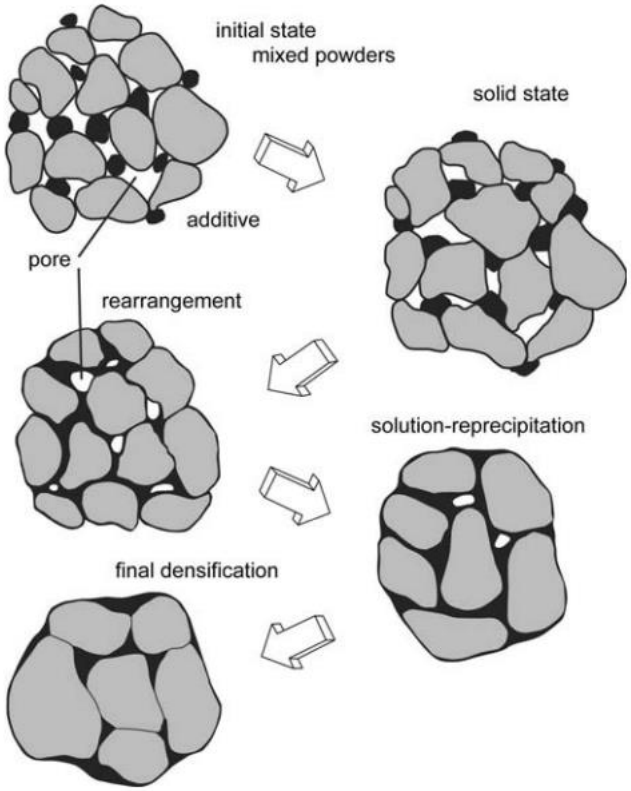

Figure 2: Schematic drawing of the microstructure changes during LPS. Reproduced from [5].

Since most microstructural studies on grain growth of ceramics were done after both sintering and grain growth, there is no consensus on the influence of liquid phases on grain growth of ceramics.

1.1.3 Field Induced Sintering

New sintering techniques were developed for faster and better densification and to suppress grain growth. Various techniques utilizing electromagnetic fields enable the fabrication of nanostructured ceramics, with finer control over the densification process [6,7].

In spark plasma sintering (SPS), the porous body is hot pressed, and heating of the sample is accomplished by passing an electric current through the die (and/or through conductive samples). The basic configuration is shown in Figure 3. The combination of rapid heating with the application of high mechanical pressure leads to very fast densification at temperatures that,

typically, are a few hundred degrees lower than those used for normal hot pressing. This has been demonstrated for conductive and non-conductive powders [8].

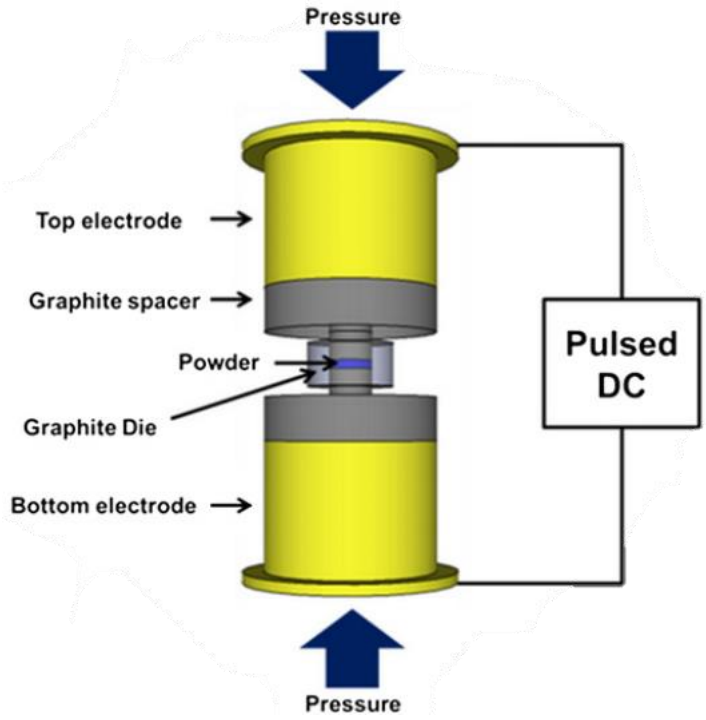

Figure 3: Schematic illustration of the SPS configuration, reproduced from [7].

In FLASH sintering, the green body is connected between two electrodes and heated in a furnace to a critical temperature, and then a DC electric current is passed through the specimen using the electrodes at a voltage larger than that used in SPS [7]. The densification of the green body in FLASH happens in extremely short times.

Induction sintering is a technique to indirectly heat *conductive* materials. An external coil passing alternating currents creates a fluctuating electromagnetic field that induces a voltage in the sample (see Figure 4). This voltage produces circulating currents (called eddy currents) that produce Joule heating of the material. If the sample itself is not conducting, it can be placed in a conductive crucible, for example, made of graphite [6]. Induction furnaces operate at frequencies in the range of 60–1,000 Hz and can reach temperatures of about 3000°C. Microwave sintering is an application of induction heating using higher frequencies. Heat is generated in nonconducting materials when microwave radiation excites the atoms in the material [7,9].

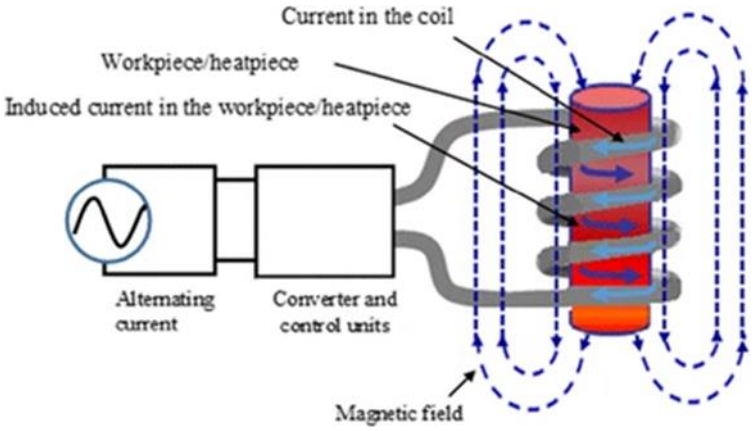

Figure 4: Schematic drawing of the induction sintering configuration [9].

1.2 Grain Boundary Mobility and Grain Growth

1.2.1 Grain Growth

The main part of grain growth occurs at the final stages of densification. In order to reduce the grain boundary area, hence decreasing the excess energy in the system, grain boundaries migrate. This is a short diffusion process where atoms move across the grain boundary and change their orientation from that of the crystal decreasing in size to that of the growing grain. The flux of atoms is thus in the opposite direction of grain boundary movement. The driving force for migration is usually expressed as the grain boundary curvature, which creates a difference in the chemical potential due to a pressure difference between the two grains so convex grains have higher chemical potential than concave grains [10]:

$$\Delta P = \gamma_{GB}\left(\frac{1}{r_1} + \frac{1}{r_2}\right) = \frac{n\gamma_{GB}}{\mathrm{G}} \qquad (2)$$

where ΔP is the pressure difference between two adjacent grains, γ_{GB} is the grain boundary energy, n is a geometric factor and G is the grain size.

1.2.2 Grain Growth Mechanism

As Equation 2 describes, the driving force for grain boundary migration is described by the difference in curvature between two adjacent grains, so the boundary will move toward the curvature center of the convex grain. (Figure 5).

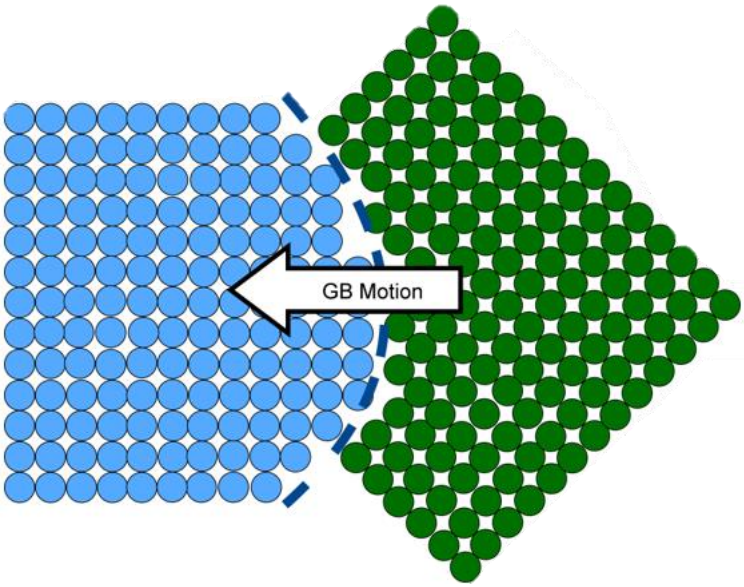

Figure 5: Schematic drawing of grain boundary migration from a concave to a convex grain [11].

As microscopy techniques improved, grain boundaries were found to be not curved, but faceted. Gleiter suggested an atomistic migration mechanism based on the terrace-ledge-kink (TLK) model for surfaces [12]. The mechanism is the lateral motion of linear defects in the plane of the grain boundary. These defects can have both a step and/or a grain boundary dislocation character and are called disconnections [13]. Atoms from the steps of the shrinking grain adsorb to the steps of the growing grain. While this model was based on the growth of a crystal from the liquid or vapor phase, it was applied for grain growth. Sternlicht et al. demonstrated using TEM that anisotropic disconnection motion is the mechanism of grain growth (in $SrTiO_3$ polycrystals) [14].

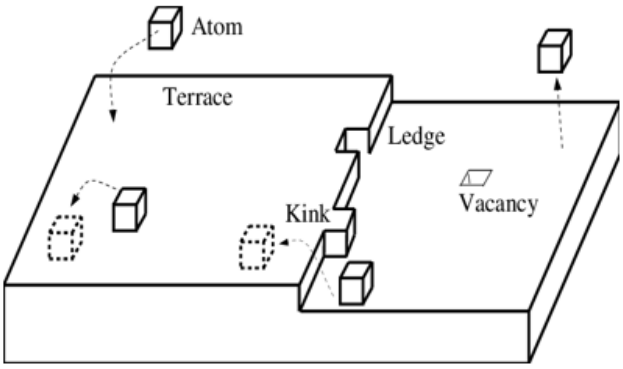

Figure 6: TLK model for describing atom motion on surfaces. Reproduced from [15].

1.2.3 Grain Boundary Mobility Measurements

The mobility of a grain boundary is defined as the velocity of grain boundary movement V_{GB} normalized by the driving force F_{GB}, in a single-phase material with unpinned grain boundaries [16].

$$M_{GB} = \frac{V_{GB}}{F_{GB}} \tag{3}$$

V_{GB} and F_{GB} depend on each other and can significantly change in the same system due to difference in grain size, changing the driving force for grain growth, hence changing the grain boundary velocity. A change in mobility can indicate a change in grain growth or grain boundary migration mechanism.

Grain boundary mobility can be determined from the measured grain size as a function of annealing time, assuming equiaxed grains and $n = 2$ [16]:

$$V_{GB} = \frac{d\bar{G}}{dt} = \frac{2M_{GB}\gamma_{GB}}{\bar{G}} \tag{4}$$

Integrating equation (4) produces the parabolic normal grain growth law:

$$\bar{G}_t^2 - \overline{G_{t=0}}^2 = 4M_{GB}\gamma_{GB}t = kt \tag{5}$$

where $\bar{G}_t^2$ is the average squared grain size at time t, $\overline{G_{t=0}}^2$ is the average squared grain size at t=0 and k is the rate constant.

Since measuring the grain boundary energy is very challenging, the term effective mobility can be derived from equation (5) as:

$$M_{GB}\gamma_{GB} = \frac{k}{4} \tag{6}$$

Plotting a graph of the average grain size as a function of annealing time at a defined temperature, and by using equations (4) and (5), the rate constant K (the slope) can be converted to the effective grain boundary mobility using equation (6).

1.2.4 Solute Drag/Acceleration

Polycrystals can have dopants or impurities in solid solution. When their concentration is below the solubility limit of the material, those dopants and impurities can undergo equilibrium (Gibbsian) segregation to the grain boundaries, if a chemical excess of the dopant reduces the grain boundary excess energy in the system. In Gibbsian segregation theory, grain boundaries are projected to one plane, but in fact solute atoms can be adsorbed to a few atomic monolayers of material. The result is a "cloud" of solute concentration at the grain boundary. When the grain boundary is stationary, this cloud can be symmetrical so the interaction forces between the solute and the grain boundary in each side of the grain boundary balance each other out. Asymmetric solute profile occurs since the diffusivity of the solute atoms across the boundary is expected to be different from that of the host material when the grain boundaries starts to move. This asymmetry can result in a drag force F_s which reduces the driving force for migration. If the driving force for the grain boundary migration is high enough, the boundary can break away and detach from the solute "cloud" and according to the solute drag theory will return to its intrinsic mobility (Figure 7) [17].

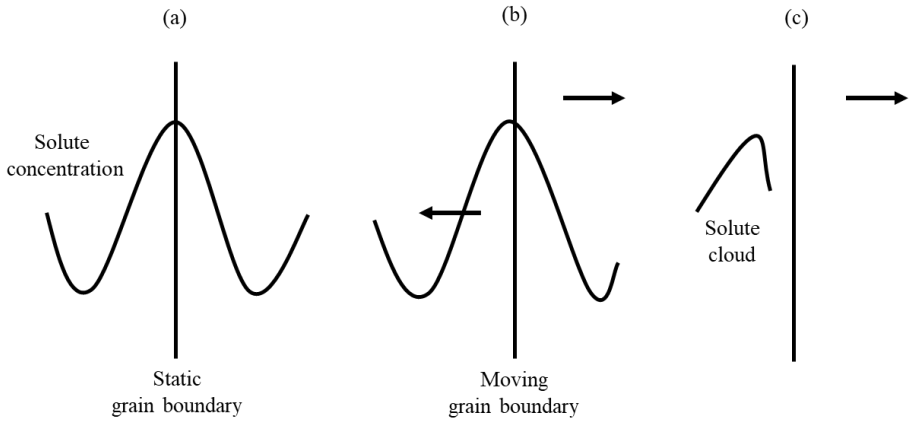

Figure 7: Schematic representation of solute drag mechanism in crystalline ceramics. (a) is a symmetrical distribution of the dopant in the region of a stationary grain boundary, (b) is an asymmetric distribution produced by the moving boundary, and (c) is breakaway of the boundary from the dopant leaving a solute cloud behind [17].

Cahn calculated the magnitude of the driving force F_s which depends on solute concentration as a function of the composition profile [18]:

$$F_s = \frac{\alpha C_\infty V_{GB}}{1 + (\beta V_{GB})^2} \tag{7}$$

where α is the solute drag force per unit velocity per unit solute concentration in the low velocity limit, C_∞ is the bulk solute concentration, V_{GB} is the grain boundary velocity and β^{-1} is the drift velocity at with which a solute diffuses across the grain boundary region. In steady state, the total drag force is assumed to be the sum of intrinsic drag force F_0 and the solute drag force F_s as described in Figure 8.

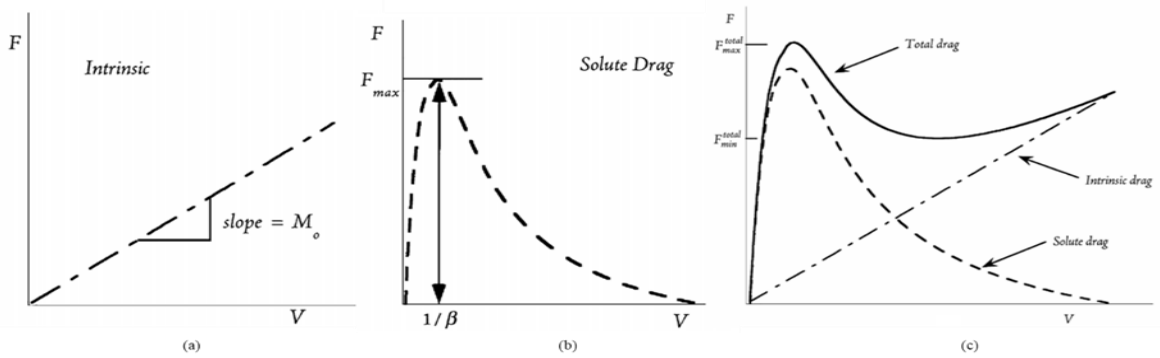

Figure 8: Driving force velocity behavior for (a) intrinsic migration (b) solute drag only and (c) total force velocity [16].

The solute drag theory doesn't explain the case where solute segregation to the grain boundary results in an *increase* of the grain boundary mobility, as has been demonstrated for a few cases in alumina and YAG [19,20,21].

1.2.5 Zener Drag

Above the solubility limit, precipitation of secondary phases occurs which can pin the grain boundaries by Zener drag (thus reducing their effective mobility) [17]. Similarly, pore interaction with grain boundaries can have the same effect [22]. This is why it is critical to work with dense materials when measuring grain boundary mobility (>95% density), where the amount of pores is insignificant,.

The first quantitative model to describe particle inhibited grain growth was developed by Zener. Assuming that the particles have a spherical shape, they are insoluble, immobile, and randomly distributed in the polycrystalline solid, the particles induce a drag force on the boundary as a pinning force:

$$F_z = \gamma_{GB} \sin(\theta) \times 2\pi r \cos(\theta) = \pi r \gamma_{GB} \cdot 2 \sin(2\theta) \qquad (8)$$

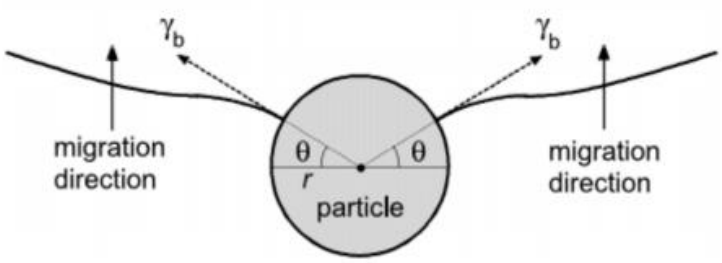

Figure 9: Interaction between a grain boundary and a second phase particle, pinning it [10].

When combined with equation ((3), the velocity of the grain boundary is reduced as to:

$$V_{GB} = M_{GB}(F_{GB} - N_z \cdot F_z) \tag{9}$$

where N_z is the particle or pore density at the grain boundary.

The velocity of the pore/particle is

$$V_p = M_p \cdot F_p \tag{10}$$

where M_p is the particle mobility.

The interaction between the grain boundary and the pore/particle can result in the following situations:

1. When $V_{GB} > V_p$, the pore will separate from the grain boundary. Separation depends on the pore's mobility.

2. When the pore migrates with the grain boundary $V_{GB} = V_p$, then $M_p \cdot F_p = M_{GB}(F_{GB} - N_z \cdot F_z)$ and a condition for Zener drag can be deduced:

$$V_{GB} = F_{GB} \cdot \frac{M_{GB}M_p}{N_z M_{GB} \cdot M_p} \tag{11}$$

This can be divided into two cases (Figure 10):

a. $F_z M_{GB} \gg M_p$ where the migration of the grain boundary will be limited (pinned) by the pore mobility, called pore control.

b. $F_z M_{GB} \ll M_p$ where the pore will not affect the grain boundary migration, called grain boundary control.

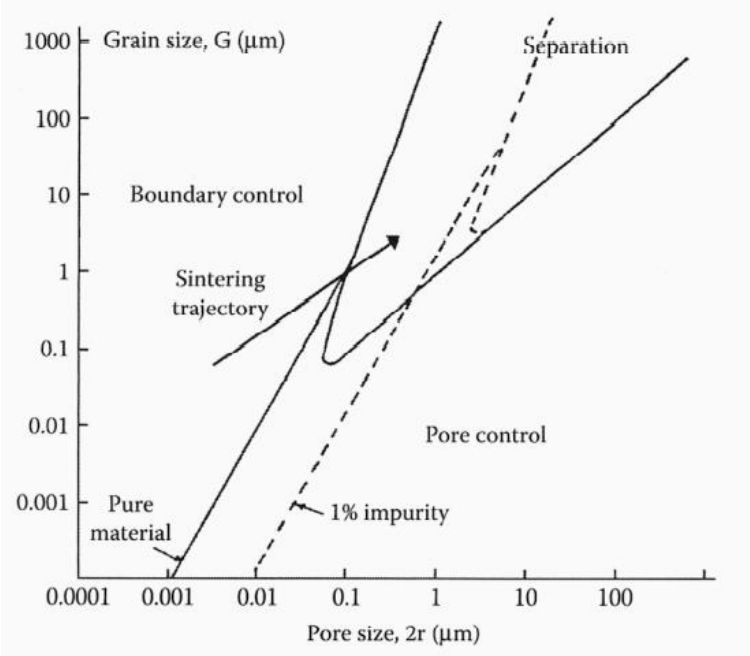

Figure 10: Pore boundary interaction as a function of grain and pore size, assuming pores migrate by surface diffusion [15].

Dopants and impurities can cause significant changes to the grain boundary mobility of materials by solute drag/acceleration and by Zener drag. Below the solubility limit, adsorbed dopant atoms can induce solute drag/acceleration on the grain boundaries mobility while above the solubility limit precipitated second phase particles will pin the grain boundaries by Zener drag, with possible influence of adsorbed solute at grain boundaries. Since it is very difficult to separate the influence of adsorbed solutes at grain boundaries from that of Zener drag, and which one of them contributes more to grain boundary drag, in a fundamental study it is preferred to work below the solubility limit.

1.2.6 Liquid Phase Effect

Grain boundary acceleration due to the presence of second phases is not reported in the literature. Overall, the effect of a liquid phase present at grain boundaries on grain boundary mobility is under debate in the ceramic community.

Grain growth in the presence of a liquid phase has been addressed by several researchers [23,24]. The proposed process occurs in three steps:

1. Dissolving of atoms from the grain into the liquid.
2. Transport of material by diffusion through the liquid phase.
3. Precipitation or attachment on the growing grain surface.

Stages 1 and 3 are known as interface reactions. Since all these steps are sequential, the slower step will be rate controlling, and hence will determine the mobility of the grain boundaries in the growing grains.

Grain growth at a rate limited by diffusion through the liquid phase can be described [25]:

$$\frac{dG}{dt} = \frac{2DS^{*}M\gamma}{kt\rho\delta R}\left(\frac{G}{G_c} - 1\right) \tag{12}$$

where S is the solubility at the surface of the solid grain, ρ is the density of the solid, M is the molecular weight of the solid phase, D is the diffusion coefficient of the solid in the liquid, γ is the solid-liquid surface energy, δ is the thickness of the liquid layer, and G_c is the critical grain radius below which the grains dissolve and above which they grow.

The rate of grain growth should decrease with an increase of liquid layer thickness δ (which can be caused by an increase in temperature or an increase of liquid content) and also by the liquid composition where D and S vary. Grain growth in the presence of a liquid phase governed by interface reaction kinetics can be described by [25]:

$$\frac{dG}{dt} = \frac{KV_m f}{kT} \tag{13}$$

where K is the interface reaction-rate constant, V_m is the molar volume, f is the driving force, k is Boltzmann's constant.

Interface reaction-controlled grain growth is independent of the thickness or volume fraction of the liquid phase and not a function of the composition of the liquid phase.

1.3 Alumina

Alumina (Al_2O_3) has a variety of metastable structures, while α-alumina is considered to be the thermodynamically stable structure of alumina [26]. α-alumina possesses a trigonal symmetry with rhombohedral Bravais centering (space group $R\,\bar{3}\,C$ (No. 167)) and has 10 atoms in the unit cell. However, it is common to represent α-alumina using a hexagonal unit cell, which following Kronberg contain 30 atoms; 12 aluminum atoms and 18 oxygen atoms (Figure 11) [27].

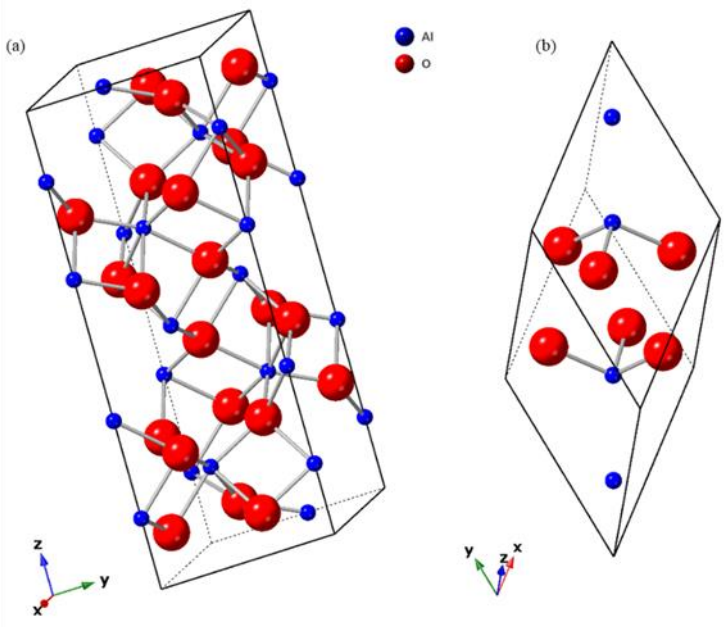

Figure 11: Schematic drawing of the hexagonal (a) and rhombohedral (b) unit cells of α-alumina. The blue spheres represent aluminum cations, and the red spheres represent oxygen anions [28].

Alumina is used in a variety of fields from bio applications to armor, because of its corrosion resistance, resistance to abrasion, reasonable fracture strength etc. It is probably the most studied ceramic, hence it is often considered a model system.

1.3.1 The Influence of Dopants on Alumina Grain Boundary Mobility

The significant effect of dopants on the processing and final properties of alumina was first shown by Coble [29], who succeeded to produce fully dense samples by adding MgO to alumina, whereas undoped alumina samples did not reach full density. Since then, additional research has shown that the addition of Mg to alumina not only increases the densification rates, but reduces the average grain boundary mobility, resulting in a finer microstructure compared to undoped alumina and also hindering abnormal grain growth [30,31,32]. Therefore, the addition of MgO to alumina is very common.

Lower alumina grain boundary mobilities resulting from the addition of Mg were reported by Bennison and Harmer [31], who showed a decrease in mobility from $1.74 \cdot 10^{-19} \frac{m^3}{s}$ for undoped alumina to $3.9 \cdot 10^{-20} \frac{m^3}{s}$ for alumina doped with 200 ppm of Mg (concentration was measured *before* sintering). Rödel and Glaeser showed a decrease in the grain growth constant K from $5.16 \cdot 10^{-20} \frac{m^3}{s}$ for undoped alumina to $1.28 \cdot 10^{-20} \frac{m^3}{s}$ for alumina doped with 250 ppm of Mg (concentration was measured *before* sintering). After Miller et al. established the solubility limit of Mg in alumina at 1600 °C to be 132±11 ppm [33], Akiva et al. measured the mobility at a Mg concentration which was experimentally confirmed to be below the solubility limit, and demonstrated a decrease in grain boundary mobility from $2.65 \cdot 10^{-15} \frac{m^2}{s}$ for undoped alumina to $1.55 \cdot 10^{-15} \frac{m^2}{s}$ for alumina doped with 23±2 ppm of Mg, due to the solute drag effect (estimated error of less than $4.2 \cdot 10^{-16}$) [34].

As opposed to Mg, doping alumina with Ca results in an *increased* grain boundary mobility and anisotropic grain growth [35,36]. Akiva et al. measured the solubility limit of CaO in alumina at 1600°C to be 51 ± 1 ppm [34]. Afterwards it was experimentally demonstrated that doping alumina with CaO below the solubility limit resulted in increased grain boundary mobility from $2.65 \cdot 10^{-15} \frac{m^2}{s}$ for undoped alumina to $3.48 \cdot 10^{-15} \frac{m^2}{s}$ for alumina doped with 13±1 ppm of Ca, contradicting the solute-drag effect which is expected when equilibrium segregation to grain boundaries occurs.

It was repeatedly shown in the literature that Ca and Si in alumina change the grain growth rate significantly and cause abnormal grain growth [37,38,39,40]. Park and Yoon [41] doped alumina samples with 100 ppm and 50 ppm of SiO_2 and Cao respectively and sintered in air at

1620°C and showed that abnormal grain growth occurs, with faceted and straight grain boundaries observed by TEM with no frozen liquid present at grain boundaries (Figure 12). They suggested that these grain boundaries have singular ordered structures with low boundary energies and their growth by lateral step movement can cause the abnormal grain growth.

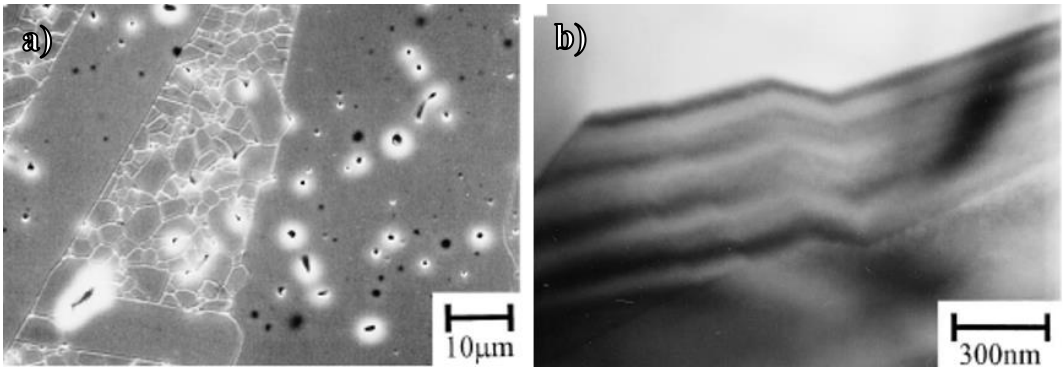

Figure 12: a) SEM micrograph of the microstructure of alumina doped with 100 ppm of SiO_2 and 50 ppm of CaO and sintered at 1620°C for 12 h; b) TEM micrograph of a faceted grain boundary. Reproduced from reference [41].

Dillon and Harmer correlated Si concentration with abnormal grain growth and reported on an adsorption transition together with a change in grain growth kinetics [40]. Together with the results of their study about Ca doped alumina [35] they demonstrated that faceting does not have a significant effect on the grain growth kinetics, but that different complexions form at the grain boundaries.

2. Research Goals

Most of the reported studies done on the mobility of alumina grain boundaries were done while densification and grain growth occurred together, and it is very difficult to separate the two different phenomena. It is therefore challenging to determine how different parameters affect the mobility of grain boundaries in alumina. Also, past studies which investigated the influence of different dopants on grain boundary mobility lacked careful measurements to determine whether their concentration is above or below the solubility limit, which might significantly affect the mechanisms that take place.

The main goal of this research program was to measure the mobility of alumina grain boundaries in fully dense samples in a field assisted, a conventional, and a graphite furnace, in order to understand the electric field effect, which is often utilized in modern sintering techniques, on the effective mobility. An additional goal was to measure the mobility in samples with different dopant concentrations, below and above the solubility limit, in order to investigate the influence of a liquid phase on the effective grain boundary mobility.

3. Experimental Methods

3.1 Sample Preparation

3.1.1 Undoped Alumina

Polycrystalline alumina samples were prepared using 150 gr of high purity (99.995%) α-Al_2O_3 powder (Ceralox HPA 0.5, Tucson, AZ), where the primary impurities declared by the manufacturer are: Na -5ppm, Si- 15ppm, Fe- 10ppm, Ca- 5ppm and Mg- 5ppm, 65 gr of distilled water, and deflocculated with 12 drops of HCl to reach a pH of about 4 and prevent agglomeration, followed by mixing for 24 hours. The samples were not intentionally doped with any material. To ensure the purity of the samples, instead of traditional slip casting of the green bodies, the green bodies were formed by vacuum filtration.

Slip casting by vacuum filtration was done by pouring the slip into a Buchner funnel connected to a vacuum pump (see Figure 13). Layers of filter paper (Whatman No. 5) were used to hold the ceramic particles but allow the water to pass through at the beginning. The flask with the Buchner funnel was connected to the vacuum pump for 5 h. Then the slip was dried in air for 24 h, and furnace dried at 80°C for 5 h and 110°C for 2 h. After drying the samples were further compacted by cold isostatic pressure (CIP) at 207 MPa.

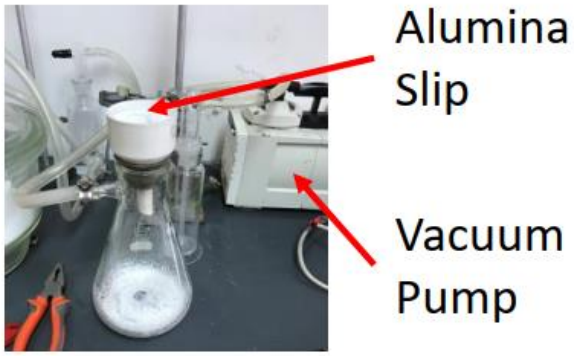

Figure 13: Photograph of the Buchner funnel used for vacuum filtration of the alumina slip.

The green bodies then underwent bisque-firing at 1000°C for 2 h in air, in order to promote necking of the alumina particles. The samples were sintered at 1600°C for 2 h in air, while covered with high purity alumina power inside the furnace, resulting in dense samples (~95% relative density).

3.1.2 Mg Doped Alumina

Polycrystalline Mg doped alumina samples were prepared using 150 gr of high purity (99.99%) α-Al_2O_3 powder (Ceralox HPA 0.5, Tucson, AZ), mixed with 1 wt% (1.5 gr) of $Mg(NO_3)_2 \cdot 6H_2O$, 65 gr of distilled water, and deflocculated with 12 drops of HCl to reach a pH of about 4 and prevent agglomeration, followed by mixing for 24 hours. The addition of Mg nitrate to the slip was done to form MgO below the solubility limit in alumina. The green bodies were formed by vacuum filtration, then the slip was dried in air for 24 h, furnace dried at 80°C for 5 hr and 110°C for 2 h. After drying the samples were further compacted by CIP at 207 MPa. The green bodies then underwent bisque-firing at 1000°C for 2 h in air. The samples were sintered at 1600°C for 2 h in air, while covered with high purity alumina power inside the furnace, resulting in dense samples (~98% relative density).

3.1.3 Laboratory RTP Alumina

Ready to press (RTP) polycrystalline alumina samples were prepared using alumina powder from Ceralox (AHPA-0.5, Sasol North America, AZ) with a purity of 99.995%, where the primary impurities declared by the manufacturer are: Na -5ppm, Si- 15ppm, Fe- 10ppm, Ca-5ppm and Mg- 300ppm. The powder was in the spray-dried, RTP form. The RTP alumina was doped with MgO (500 ppm) by the supplier. The powder was used in its as-received form. Alumina green bodies were prepared by uniaxial pressing at 41 MPa, followed by CIP at 207 MPa. The green bodies were bisque-fired at 1000°C for 2 h in air, in order to promote necking of the alumina particles and also for binder burn-out. The samples then were sintered at 1600°C for 2 h in air, while covered with high purity alumina power inside the furnace, resulting in dense samples (~99% relative density).

3.1.4 Alumina Co-doped with Ca and Si

RTP samples were prepared as mentioned above, with an additional infiltration process before the sintering stage. During the infiltration process, the bisque-fired green bodies were placed in a beaker inside a vacuum desiccator for 30 min, and then 30 ml of tetraethyl orthosilicate (TEOS) diluted in 120 ml of ethanol was added to the beaker (inside the vacuum desiccator, without breaking vacuum). Samples were held in the vacuum desiccator for ∼24 h to ensure infiltration. After 24 h, the beakers were removed from the vacuum desiccator and heated to

~60°C to reduce the contact angle of the solution with alumina and further promote infiltration [42]. The samples were then dried first at room temperature for ~12 h and then at 110°C in an air furnace for 5 h.

The samples then underwent pyrolysis in an air furnace at 700˚C for 2 h to convert the TEOS to SiO_2 in the reaction [43]:

$$Si(OC_2H_5)_4 \rightarrow SiO_2 + 2(C_2H_5)_2O \quad (14)$$

where at above 600°C diethyl ether decomposes to methane, carbon monoxide, ethylene and hydrogen gases [44].

In order to dope the green bodies with Ca, an additional infiltration process was conducted, this time with 15 wt% $Ca(NO_3)$ water-based solution. The samples then were pyrolyzed in an air furnace at 600°C for 2 h to evaporate the additional nitride solution, resulting in CaO doped samples.

The green bodies, now co-doped with SiO_2 and CaO, were sintered at 1600°C for 2 h in air, while covered with high purity alumina power inside the furnace, resulting in samples with ~95% density. BSE SEM analysis showed (Figure 14) that as result from the infiltration process, the samples contain many second phase particles. The amount of particles, combined with the relatively low density (~93%), makes the sample incompatible for mobility measurements. Additional infiltration trials with diluted solution failed to make a compatible sample, so the infiltration process deemed incompatible for this experiment.

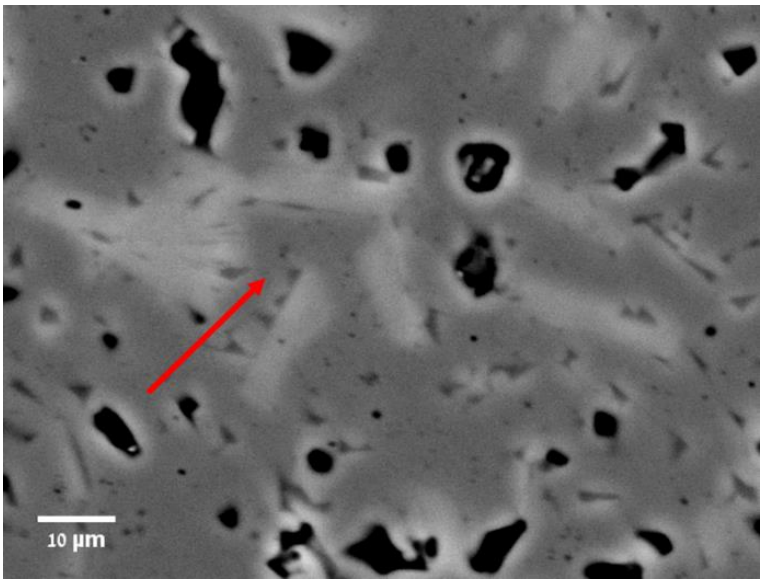

Figure 14: BSE SEM micrograph of a cross-sectioned infiltrated alumina sample containing secondary phase particles (gray), where the matrix has a dark grey contrast, and the pores have a black contrast.

3.1.5 Commercial RTP Alumina 99.5%

RTP polycrystalline alumina samples were prepared using commercial alumina powder with a purity of 99.5%. Commercial alumina green bodies were prepared by uniaxial pressing at 41 MPa, followed by CIP at 207 MPa. The green bodies underwent bisque-firing at 1000°C for 2 h in air, in order to promote necking of the alumina particles and also for binder burn-out. The samples then were sintered at 1600°C for 4 h in air, while covered with high purity alumina power inside the furnace, resulting in dense samples (~99% relative density).

3.1.6 Commercial RTP Alumina 98%

Additional RTP polycrystalline alumina samples with a higher amount of glass were prepared using commercial alumina powder with a purity of 98% supplied as pressed green body tiles (the other 2% are sintering additives, mostly containing silicone and calcium). The green bodies underwent bisque-firing at 1000°C for 2 h in air to promote necking of the alumina particles and also for binder burn-out. The samples then were sintered at 1600°C for 2 h in air, while covered with high purity alumina power inside the furnace, resulting in dense samples (~99% relative density).

3.2 Thermal Treatments

Each fully dense “mother sample” which was prepared as described in section 3.1 was cut into pieces, that were divided into groups and underwent thermal annealing in different atmospheres to promote grain growth. The chosen atmospheres were air, carbon (CO/CO_2) rich ambient and under a field, which are common in today’s sintering processes (conventional sintering in air and field-assisted sintering techniques that usually utilize graphite crucibles).

Samples were annealed in a conventional air furnace for 1min, 1 h, 2 h, 5 h, 10 h and 12 h. For the CO/CO_2 rich atmosphere, samples were annealed in a high-temperature resistance furnace with graphite heating elements and crucibles under flowing He (99.995%) for 1min, 1 h, 2 h, 5 h, 10 h and 12 h. Samples were annealed in a field assisted furnace in an Ar ambient under an alternating field for 30 sec, 5 min, 30 min, 1 h and 4 h.

Table 1: List of thermal treatments conducted for each of the samples studied in this research.

Sample	**Air Furnace**	**Graphite Furnace**	**Field Assisted Furnace**
Undoped	1min, 1h, 2h, 5h, 10h, 12h	1min, 1h, 2h, 5h, 10h, 12h	30sec, 5min, 30min, 1h, 4h
Mg doped	1min, 1h, 2h, 5h, 10h, 12h	1min, 1h, 2h, 5h, 10h, 12h	30sec, 5min, 30min, 1h, 4h
RTP	1min, 1h, 2h, 5h, 10h, 12h	1min, 1h, 2h, 5h, 10h, 12h	30sec, 5min, 30min, 1h, 4h
Commercial 99.5%	1min, 1h, 2h, 5h, 10h, 12h	1min, 1h, 2h, 5h, 10h, 12h	30sec, 5min, 30min, 1h, 4h
Commercial 98%	1min, 1h, 2h, 5h, 10h, 12h	-	-

3.3 Characterization

3.3.1 Density

The density of each mother sample was measured using the Archimedes method following ASTM standard c 20-92, to make sure they are above the desired relative density of 95%:

$$\rho = \left(\frac{D}{W - S}\right) \cdot \frac{1}{\rho_{Al_2O_3}} \tag{15}$$

where ρ is the relative density, D is the dry weight, W is the saturated weight, S is the suspended weight and $\rho_{Al_2O_3}$ is the theoretical density of alumina which is 3.97 gr/cm^3.

3.3.2 Wavelength Dispersive Spectroscopy

The Mg, Ca and Si concentration in each sample was measured using wavelength dispersive spectroscopy (WDS; Oxford Instruments, High Wyecombe, U.K.) mounted on a SEM (FEI Quanta 200). A SEM accelerating voltage of 30 kV and a constant electron beam current of ~60 nA were used for WDS experiments. The measurements were acquired at a working distance of 11 mm with a measurement time of 20 s. A polyethylene terephthalate (PET) crystal was used as a monochromator for the WDS measurements of Ca and Si and thallium acid phthalate (TAP) crystal for the measurements of Mg. Diopside ($MgCaSi_2O_6$) crystal was used as a

standard for Mg, Ca and Si quantification. The appropriate K_α peak was measured at a spectral position showing a maximum intensity. The background intensity was measured at two different spectral positions around the peak position. The background intensity at the peak position was calculated using linear interpolation. 30 measurements were taken from random locations across the cross section for each element quantification.

The dopant's concentration was calculated according to:

$$C = k \cdot C_{std} \cdot g_{ZAF} \tag{16}$$

where C_{std} is the concentration of the standard (for a pure element C_{Std}=1), k is a constant describing the ratio between the intensities of the peak and its background and g_{ZAF} correlates to the ZAF correction factor, where Z is the atomic number correction, A is the absorption correction, and F is the characteristic fluorescence correction. For the dopant content measurements, a ZAF correction factor was calculated using XPHI Software [45].

The limit of detection was determined using [45]:

$$C_{\mathrm{lim},0.975} = C_{std} \cdot g_{ZAF} \cdot \frac{2\sqrt{2I_{background}}}{\sqrt{m\tau} \cdot I_{std}} \tag{17}$$

where $C_{lim,0.975}$ is the limit of detection with a confidence probability of 97.5%. $I_{background}$ is the background intensity, C_{std} and I_{std} are the concentration and intensity from a standard with a known concentration, respectively, m is the number of measurements, and τ is the measurement time.

3.3.3 X-ray Diffraction

X-ray diffraction (XRD) was used to identify additional phases in the alumina samples. XRD patterns were acquired using a X-ray powder diffractometer (Rigaku Smart Lab X-ray Diffractometer, Tokyo, Japan) with a Cu Kα rotating anode, operated at 200mA and 45 kV, with 0.3 mm receiving slits. Diffraction patterns were acquired at steps of 2θ = 0.01° and 1.2 s/step exposure.

3.3.4 Scanning and Scanning/Transmission Electron Microscopy

Scanning electron microscopy (SEM) and scanning/transmission electron microscopy (S/TEM) were used to characterize the microstructure of the different alumina samples. SEM was conducted using a FEI Quanta 200 E-SEM (Eindhoven, Holland) and a Zeiss Ultra-Plus field emission gun SEM (Oberkochen, Germany). S/TEM was conducted using a Tecnai T-20 G2 at 200 kV (FEI, Eindhoven, Holland) and a monochromated and double aberration-corrected S/TEM (FEI Themis-Z 80–300 keV S/TEM) operated at 300 kV, to confirm the presence of a second phase in the commercial RTP sample. Chemical analysis of the second phase found at triple junctions and grain boundaries were conducted using STEM - EDS (EDAX, Tilburg, Holland).

3.3.5 Grain Size Analysis

Grain sizes were measured using a MatLab program following the linear intercept method [46], from 600-1500 grains in each sample. A correction factor of 1.57 was used to correlate between the average grain size $\bar{G}$ and the average intercept length $\bar{L}$, so $\bar{G} = 1.57 \cdot \bar{L}$. Grain growth was characterized using a parabolic behavior in equation (5).

3.3.6 Specimen Preparation for Characterization

For SEM each sample was cut and an interior section was mechanically polished using a diamond suspension on polishing cloths, starting from a diamond size of 30 μm and concluding with a diamond size of 1 μm. After polishing, the samples were ultrasonically cleaned in acetone, ethanol and then rinsed in isopropanol. Thermal annealing for grain boundary grooving was conducted in an air furnace at 1250°C for 2 h.

For WDS measurements the samples were cross sectioned and then polished using the same process conducted for the SEM samples, without thermal (or chemical) etching to prevent possible changes in concentration.

For S/TEM, samples were sliced in the form of 3 mm diameter disks, mechanically ground to a thickness of ~100 μm, mechanically dimpled to a thickness of about ~30 μm and ion milled to perforation with Ar at 4–8 kV using a Gatan 695 Precision Ion Polishing System (PIPS-II).

Focused ion beam (FIB, Helios 5 PFIB CXe) was used to cross section the commercial RTP alumina 99.5% samples for subsequent characterization of the near surface region.

3.3.6.1 Wear Rate

To evaluate the wear resistance of the specimens, diamond-cutting experiments using a precision cut-off machine (Minitom, Struers, Cleveland, USA) with diamond wafer blades were conducted. In these experiments, specimens of identical cross-sectional area were cut with a diamond wafer blade for a specifically defined time (7 or 10 min); under identical load conditions. The specimens were not fully sectioned, but rather the depth of each cut after the defined cutting time was measured. The wear rate was expressed as the cross-sectional cut area, which is the length of the cut multiplied by the specimen's width, divided by the cutting time. The experiments were performed under a load of 100 g and rotational speed of 150 rpm using a 0.3 mm thick wafering blade (IsoMet Diamond Wafering Blades, Buehler, Lake Bluff, USA) with a diameter of 102 mm. The width of the specimens was between 7.95 mm and 8.78 mm. The diamond wafer blade was dressed during the experiment every 2 min. Three cuts were performed per specimen, and optical microscopy was used to measure the depth of the cut. SEM and EDS was used to characterize the sliced surface and chemistry.

4. Results

4.1 Phase Analysis

Dopants can have a significant effect on the microstructure of the sintered samples, e.g. Ca is known to cause abnormal grain growth. Thus, it is important to know the exact amount of impurities and dopants in the samples to fully understand their influence on grain growth. During processing of the samples, impurities can be introduced even at trace levels from the starting powder, the molds, furnaces and other lab equipment. Also, dopants added in solution or mixed into the powder might evaporate during sintering, hence changing the intentionally added dopant concentration.

An effort to measure the actual concentration of key dopants (Ca, Mg, Si) in the "mother" samples below the solubility limit was conducted by WDS after sintering. The solubility limit of Ca, Mg and Si in alumina at 1600°C is 51 ppm, 132 ppm and 188 ppm respectively [33,34,47]. In addition, samples containing dopants above solubility limit were characterized by XRD and STEM EDS or back scattered SEM.

4.1.1 Undoped Alumina

The density of the sintered sample was determined using the Archimedes method, resulting in 95.3% of the theoretical density, which is just above the desired density. The amount of Ca, Mg and Si was determined using WDS, and the results are presented in Table 3 showing 6±15 ppm of Mg with a detection limit of 3 ppm and 7±17 ppm of Ca with a detection limit of 6 ppm, which are below the solubility limit in alumina and corresponds with the base-purity of the starting powders, as specified by the supplier. The Si concentration in the sample was determined to be 49±19, which is above the specified base-purity (20 ppm) but still below the solubility limit of Si in alumina at 1600°C. The microstructure of the undoped sample is presented in Figure 15.

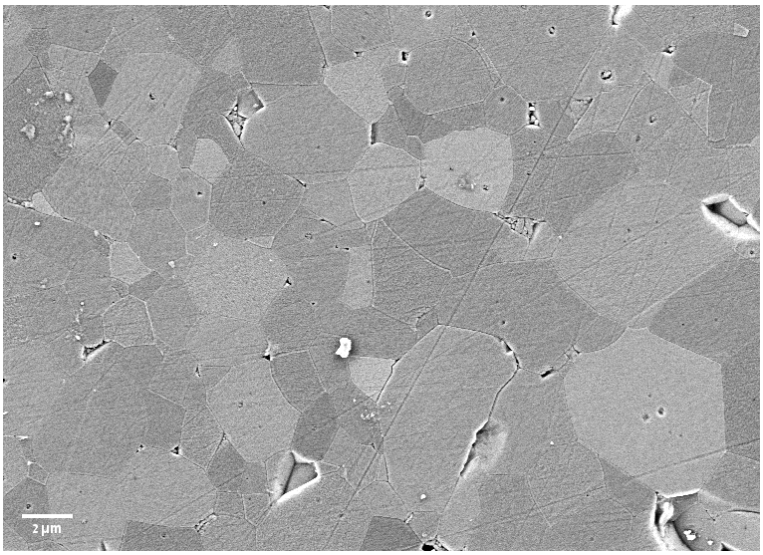

Figure 15: SE SEM micrograph of the microstructure of undoped alumina sintered for 2 h.

4.1.2 Mg Doped Alumina

The density of the sintered sample was determined using the Archimedes method, resulting in 98.0% of the theoretical density. The amount of Ca, Mg and Si was determined using WDS, and the results are presented in Table 3 showing 11±5 ppm of Ca at a detection limit of 3 ppm and 55±30 ppm of Si at a detection limit of 9 ppm, which are below the solubility limit in alumina at 1600°C. The Mg concentration in the sample was determined to be 45±19 at a detection limit of 19 ppm, showing that the doping process succeeded. The microstructure of the Mg doped sample is presented in Figure 16.

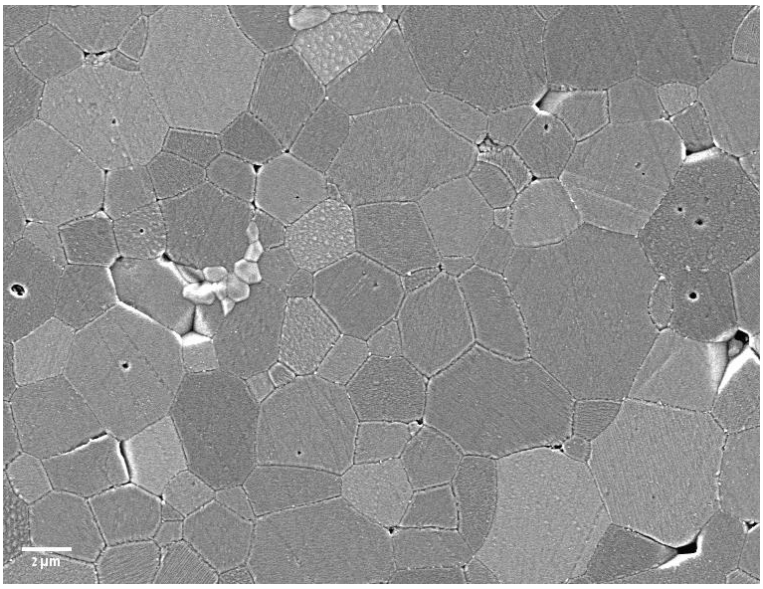

Figure 16: SE SEM micrograph of the microstructure of Mg doped alumina sintered for 2 h.

4.1.3 RTP Alumina

The density of the sintered sample was determined using the Archimedes method, resulting in 99.6% of the theoretical density. The amount of Ca and Si was determined using WDS, the results are presented in Table 3, showing 29±33 ppm of Ca at a detection limit of 2 ppm and 54±18 ppm of Si at a detection limit of 9 ppm, which are below the solubility limit in alumina at 1600°C. The base-purity of the starting powders, as specified by the supplier, is 10 ppm of Ca and 105 ppm of Si. The specified amount of Mg was 300 ppm, which is above the solubility limit in alumina at 1600°C. Mg was added to the powder by the supplier by the addition of high purity magnesium aluminate spinel. The microstructure of the Mg doped sample is presented in Figure 17, showing negligible amount of Mg spinel particles.

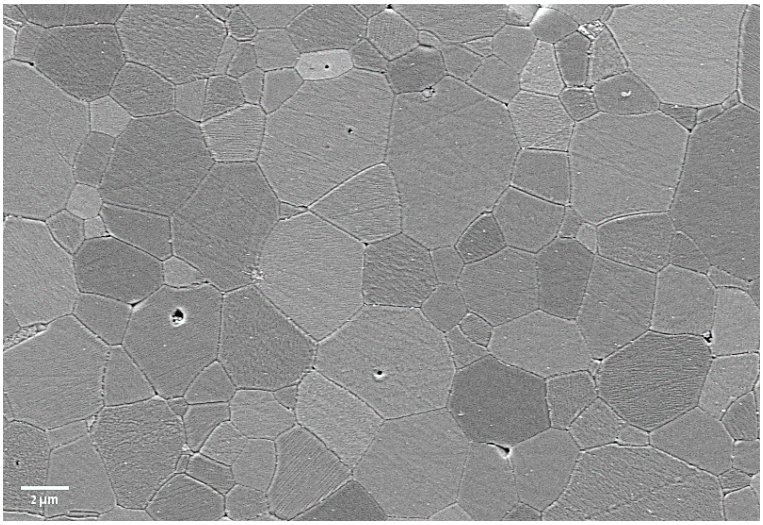

Figure 17: SE SEM micrograph of the microstructure of RTP alumina sample sintered for 2 h.

4.1.4 Commercial RTP Alumina 99.5%

The density of the sintered sample was determined using the Archimedes method, resulting in 99.3% of the theoretical density. The amount of Mg, Ca and Si in the 99.5% alumina powder is above the solubility limit so WDS (or EDS) cannot be used to measure them. XRD acquired from the sample (Figure 18) shows only alumina peaks and no other phase could be detected. If the second phase is amorphous it will not show any peaks in the XRD, but rather a broad signal at low scattering angles. The absence of peaks from a crystalline second phase might be due to the limited X-ray detection limit.

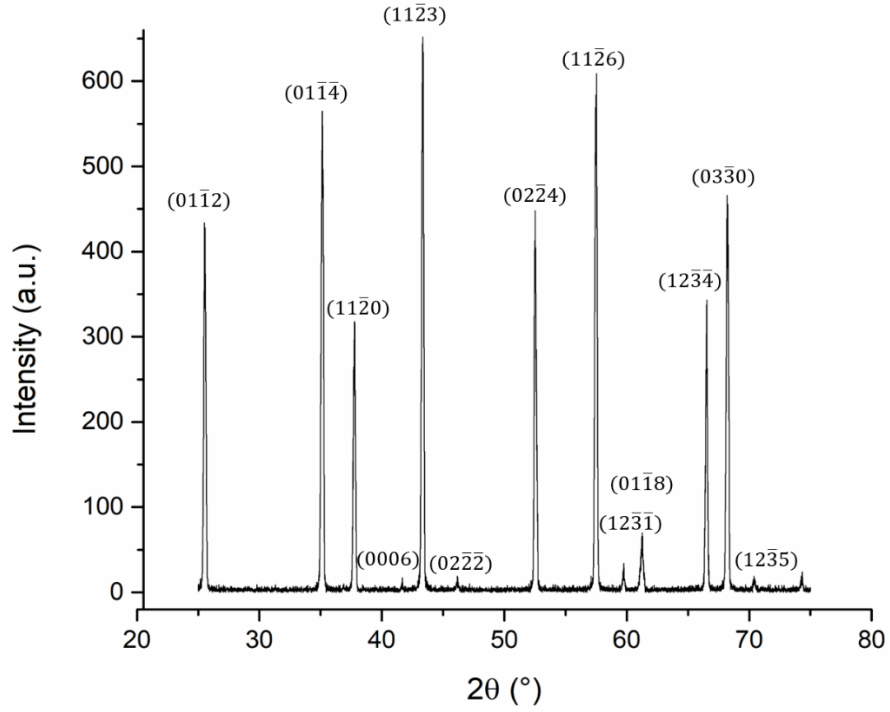

Figure 18: XRD pattern of commercial RTP alumina sample containing 0.5% of glass, presenting only alumina reflections. Reflections from a second phase were not detected.

STEM was used to analyze the second phase (dopants are above solubility limit). HAADF STEM (Figure 19) showed a darker contrast at triple junctions and some of the grain boundaries, while a phase containing heavier elements such as Mg, Si and Ca should appear brighter due two larger scattering, meaning the suspected areas might be holes in the sample and not a second phase.

Analysis done in STEM-EDS (Figure 20) revealed the presence of Mg, Ca, Si and Na in those areas, meaning the second phase might have been preferentially milled during ion-milling so it appears darker in the HAADF-STEM micrograph.

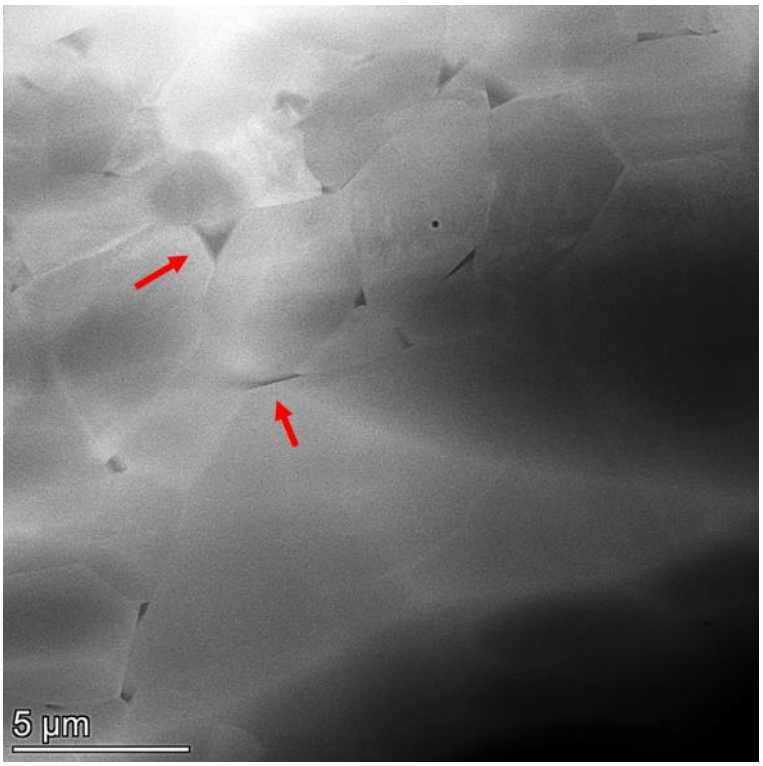

Figure 19: HAADF STEM micrograph showing second phase at triple junctions and some of the grain boundaries.

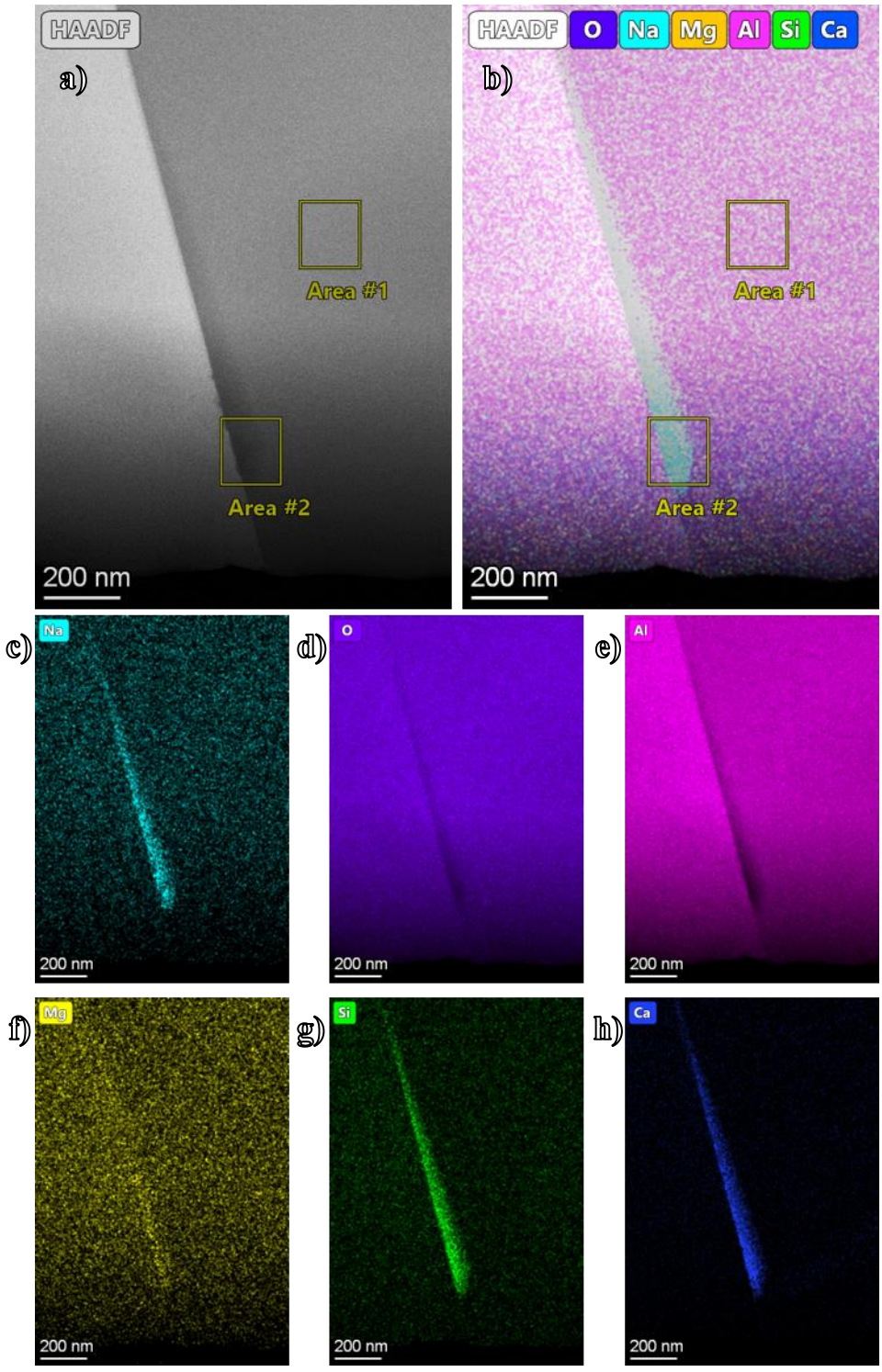

Figure 20: a) HAADF STEM micrograph of a selected area for EDS at a grain boundary. b) HAADF STEM micrograph combined with elemental EDS map. c-h) individual EDS maps at the grain boundary showing Na, O, Al, Mg, Si, and Ca.

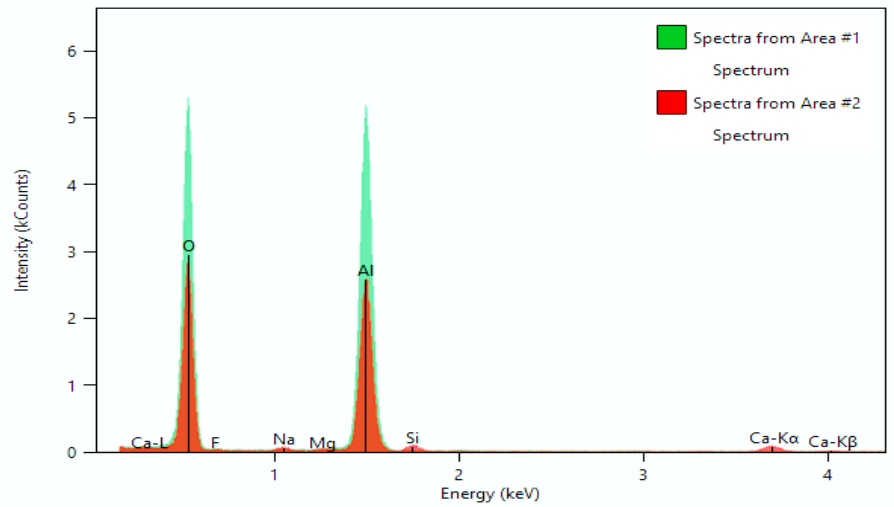

Figure 21: EDS spectrum acquired from the grain boundary indicated as areas 1 and 2 in Figure 20 .

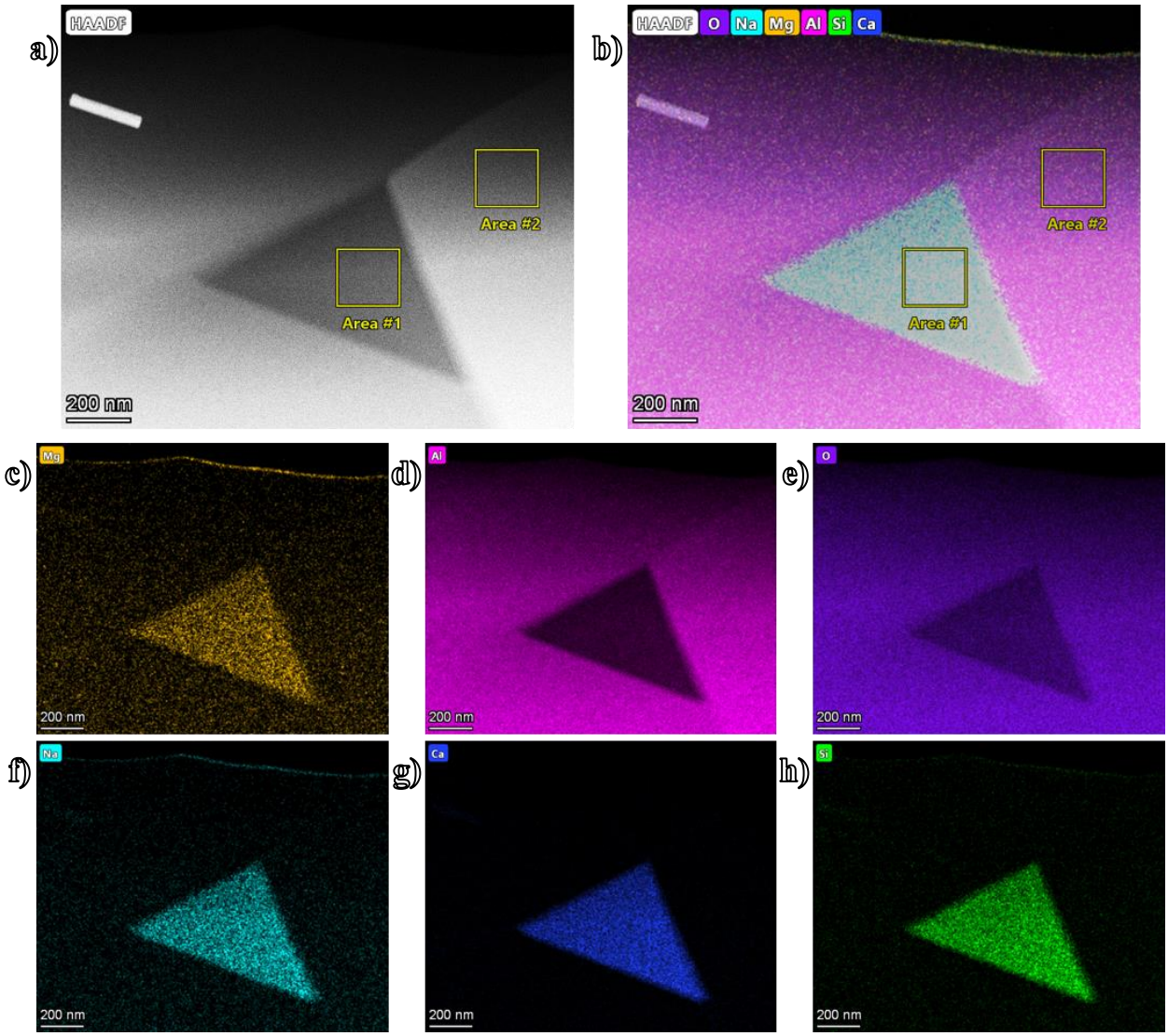

Figure 22: a) HAADF STEM micrograph of selected areas for EDS at a triple junction. b) HAADF STEM micrograph combined with elemental EDS map. c-h) individual EDS maps at a triple junction for Na, O, Al, Mg, Si, and Ca.

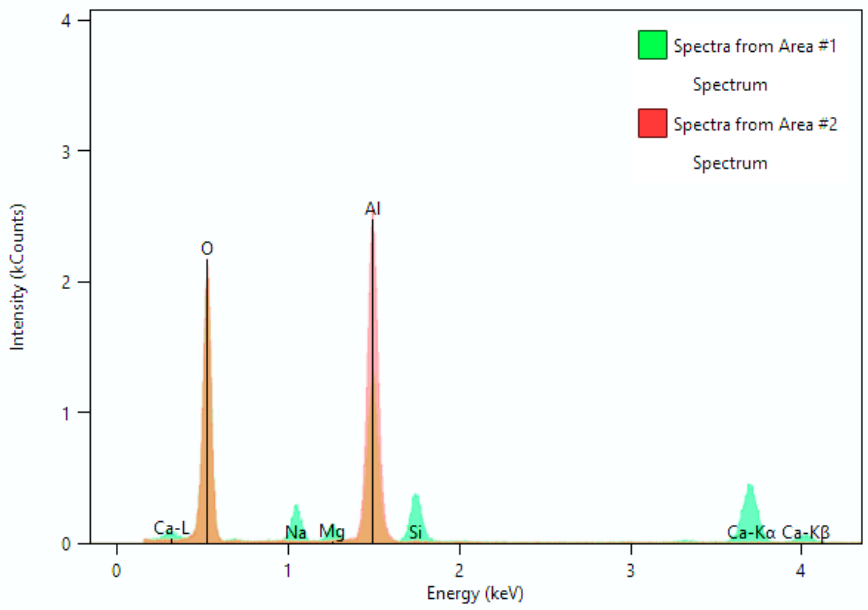

Figure 23: EDS spectrum from a triple junction in areas 1 and 2 in Figure 22.

Electron diffraction acquired from the second phase at a triple junction (Figure 24a) shows diffuse rings, meaning that the second phase is amorphous. All d-spaces in Figure 24b correlate to alumina planes. A SEM micrograph shows the microstructure of the sintered sample in Figure 25.

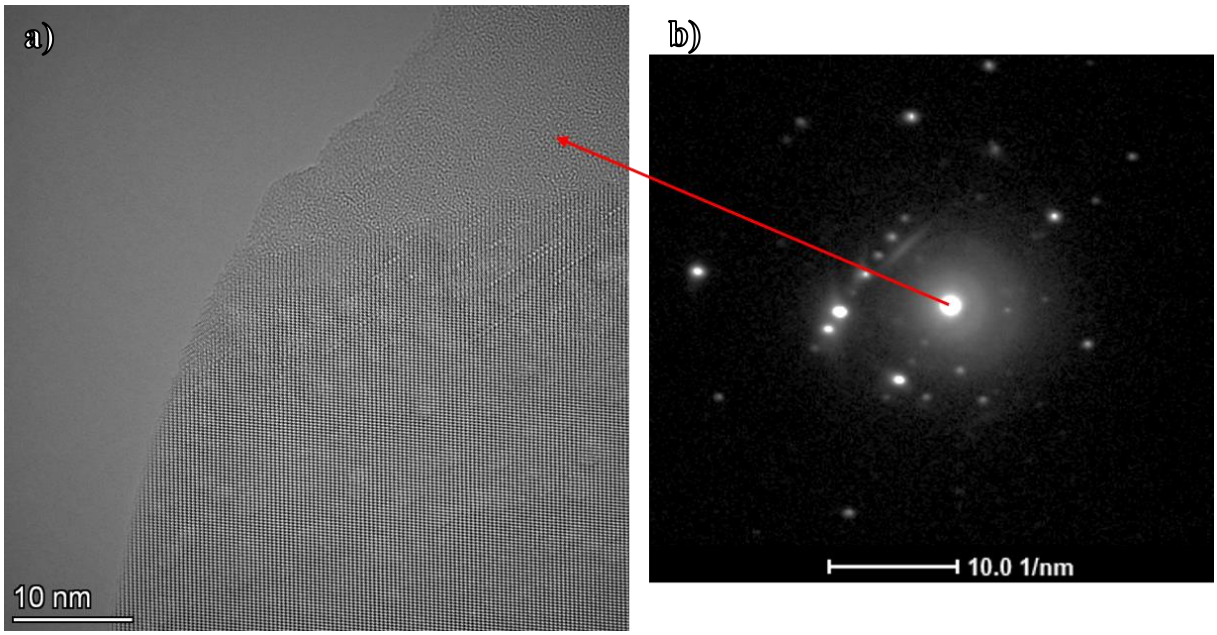

Figure 24- a) HRTEM micrograph of commercial RTP alumina sample edge, showing a crystalline alumina grain below an apparently amorphous area. b) Electron diffraction pattern acquired from the apparently amorphous area in a, showed diffuse rings, confirming it is amorphous.

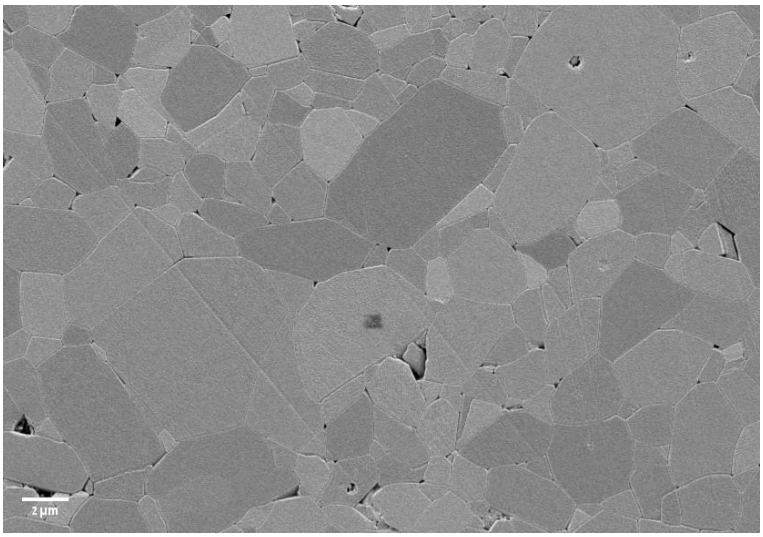

Figure 25: SE SEM micrograph of the microstructure of commercial RTP alumina sample sintered for 4 h.

4.1.5 Commercial RTP Alumina 98%

The density of the sintered sample was determined using the Archimedes method, resulting in 98.8% of the theoretical density, taking into consideration 2% glass content in the sample with a theoretical density of anorthite glass of 2.75 gr/cm^3 [48]. The amount of Mg, Ca and Si in the 98% alumina powder is above the solubility limit so WDS cannot be used to measure them. XRD taken from the sample (Figure 26) shows only alumina peaks and no other phase could be detected. BSE SEM micrograph (Figure 27) shows a brighter contrast, indicating a second phase. EDS shown in Table 2 done on the second phase (overlapping with the alumina grain) confirms the presence of the elements: Ca, Na, Mg and Si. A SEM micrograph of the microstructure of the sintered sample is presented in Figure 28.

Figure 29 shows the microstructure of the commercial RTP alumina 98% samples annealed in an air furnace for 1 h, 3 h, and 10 h. At first there are fine grains with spaces between them, then some of the grains coarsen, still surrounded by smaller grains with spaces between them and the final microstructure of coarse grains with an exuded phase between them. The sample was fully dense so the nature of the spaces between the grains at shorter annealing times can be explained by evaporation of the second phase during thermal etching (which is present at the grain boundaries after polishing as can be seen in Figure 27a,b). As grains grow, the second phase layer thickness increases and there are still some second phase left at grain boundaries after thermal etching.

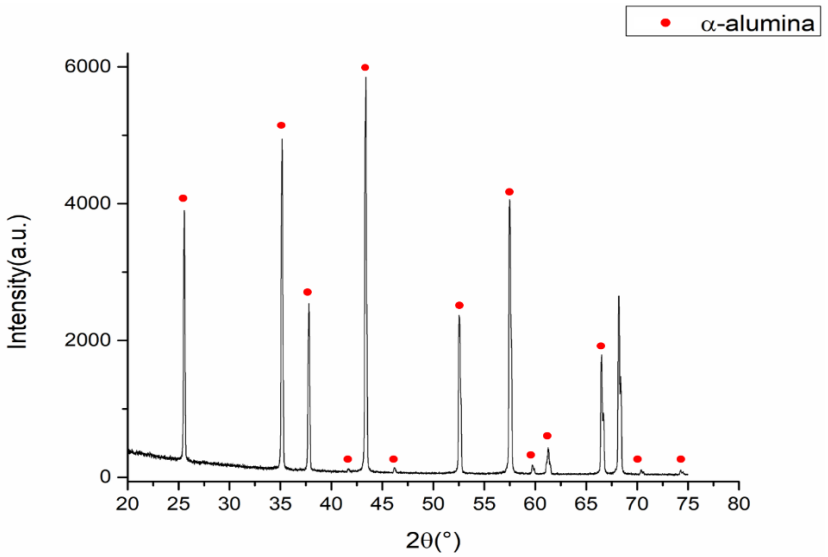

Figure 26: XRD pattern of commercial alumina sample containing 2% of glass, presenting only alumina reflections. Reflections from a second phase were not detected.

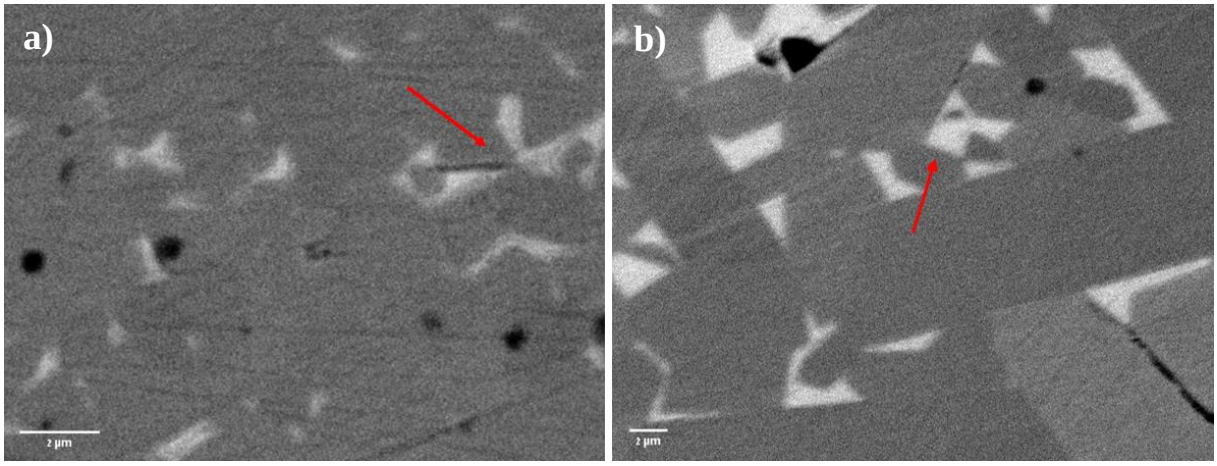

Figure 27: BSE SEM micrograph showing a second phase (marked with arrow) in the commercial 98% alumina sample annealed for a) 1 min and b) 10 h in an air furnace, polished without thermal etching.

Table 2: EDS measurements of the second phase (Figure 27a, marked in arrow) overlapping with alumina grain, showing the elemental distribution.

Element	**wt.%**
O	50.72
Al	42.49
Si	3.09
Ca	2.26
Na	1.05
Mg	0.38

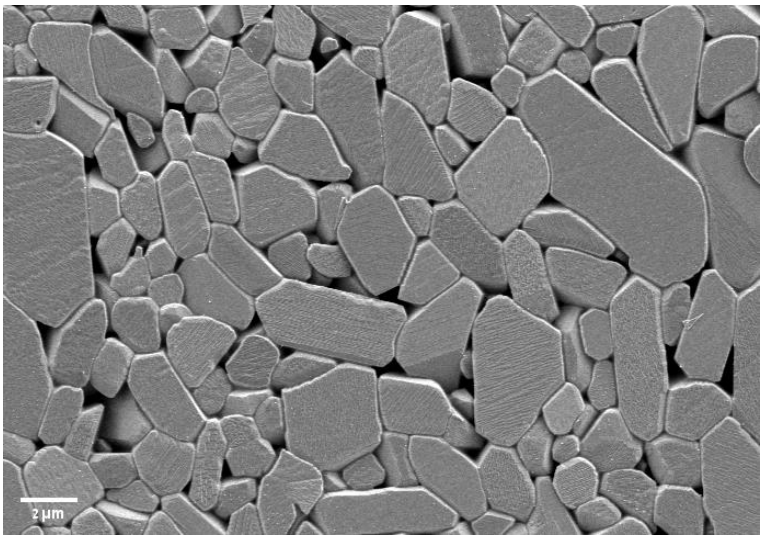

Figure 28: SE SEM micrograph of the microstructure of a commercial 98% alumina sample sintered for 2 h.

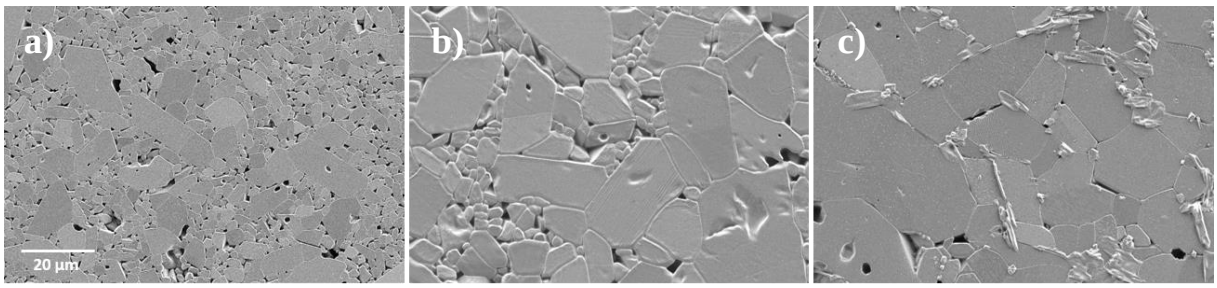

Figure 29: SE SEM micrograph of the microstructure evolution of the commercial 98% alumina samples, annealed in an air furnace for: a) 1 h, b) 3 h, and c) 10 h.

Table 3 summaries the properties of all samples prepared from for the grain growth experiments, from which all samples for the annealing experiments were cut.

Table 3: Summary of the dopant/impurity concentration of the samples.

Sample	Dopant	Concentration [ppm]	Detection limit [ppm]	Below/above solubility limit	Relative density
Undoped	Mg	6 ± 15	3	Below	95.3%
	Ca	7 ± 17	6	Below	
	Si	49 ± 19	11	Below	

Mg doped	Mg	45 ± 19	19	Below	98%
	Ca	11 ± 5	3	Below	
	Si	55 ± 30	9	Below	
RTP	Mg	> 132	-	Above	99.6%
	Ca	29 ± 33	2	Below	
	Si	54 ± 18	9	Below	
Commercial RTP 99.5%	Mg	> 132	-	Above	99.3%
	Ca	> 51	-	Above	
	Si	> 188	-	Above	
Commercial RTP 98%	Mg	> 132	-	Above	98.8%
	Ca	> 51	-	Above	
	Si	> 188	-	Above	

4.2 Grain Boundary mobility of alumina at 1600°C

4.2.1 Microstructure

The microstructure of the undoped and doped polycrystalline alumina samples annealed for one hour in an air furnace, a graphite furnace and a field assisted furnace at 1600°C are presented in Figure 30. The undoped, Mg doped and RTP alumina samples (Figure 30a-c), that do not contain a second glassy phase, exhibited equiaxed grain growth in all furnaces. Commercial RTP with 99.5% alumina (Figure 30d), that contained a glassy phase, exhibited larger grains surrounded by smaller ones, suggesting that the grains grow by grain coarsening.

Compared to conventional annealing in an air furnace, samples that were annealed in a graphite furnace exhibit a finer microstructure. Samples that were annealed in a field assisted furnace exhibit a much coarser microstructure with large pores. In addition, the commercial RTP alumina sample exhibits a second phase exuded from the grain boundaries.

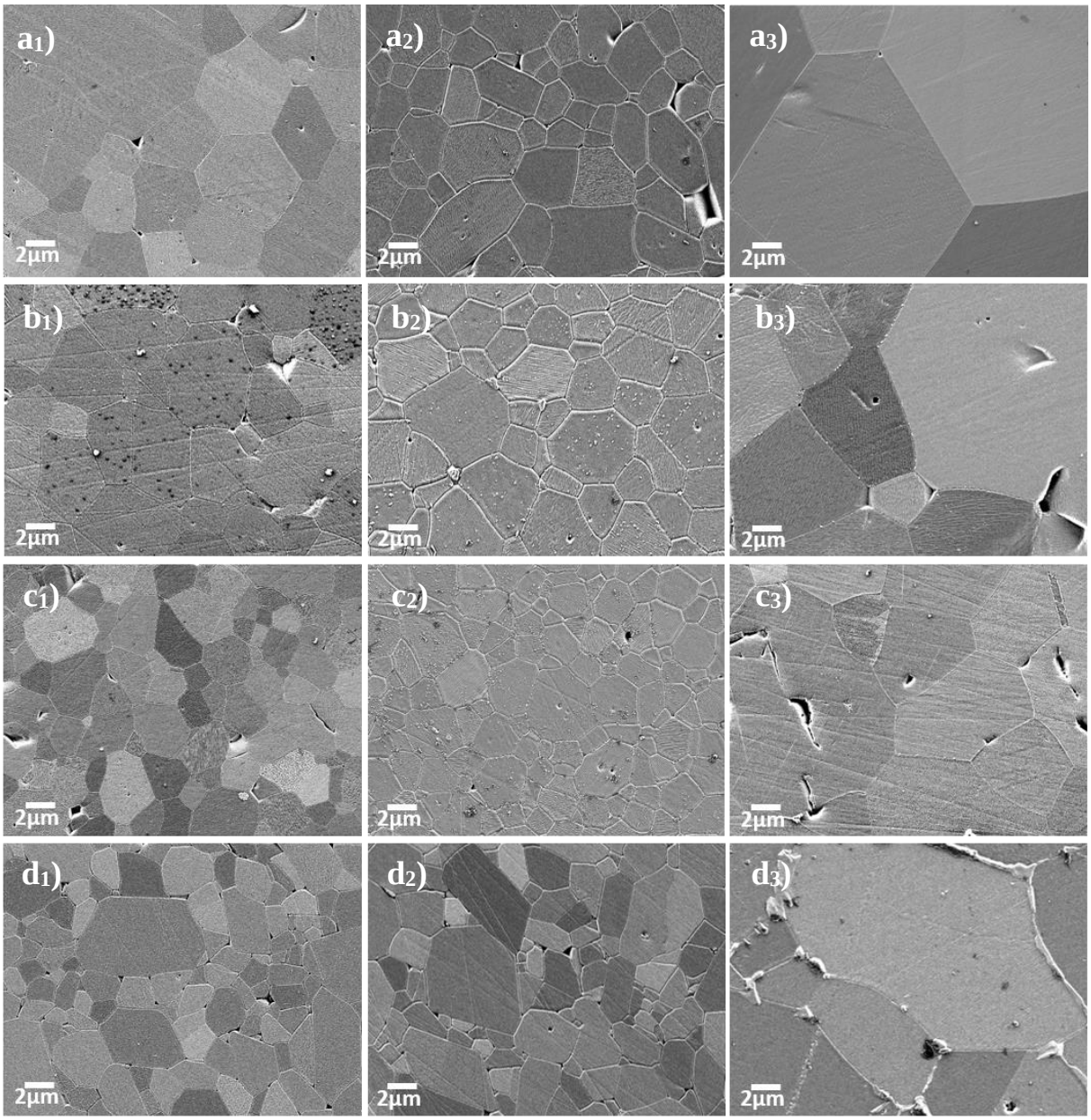

Figure 30: SE SEM micrographs of the microstructure of: a) undoped alumina; b) Mg-doped alumina; c) RTP alumina; d) commercial RTP alumina annealed for 1 h at 1600°C in 1- air furnace; 2- graphite furnace; or 3- field assisted furnace.

Based on the measured grain size, the grain growth rate is plotted in Figure 31 and Figure 33, showing the different growth rates of the alumina samples with different doping in the different furnaces.

4.2.2 Grain Growth: Composition Effect

Samples of different compositions annealed in the different furnaces all show similar trends. The undoped samples exhibit much faster growth rates than the doped samples. When a second glassy phase is present, the samples annealed in an air and a field assisted furnaces have higher growth rates than the samples doped below solubility limit but still lower than the undoped samples, where the sample annealed in the graphite furnace shows an even lower growth rate from the ones doped below solubility limit. Mg doped and RTP alumina samples show similar growth rates, where the RTP one is slightly lower, aside from the one annealed in a graphite furnace.

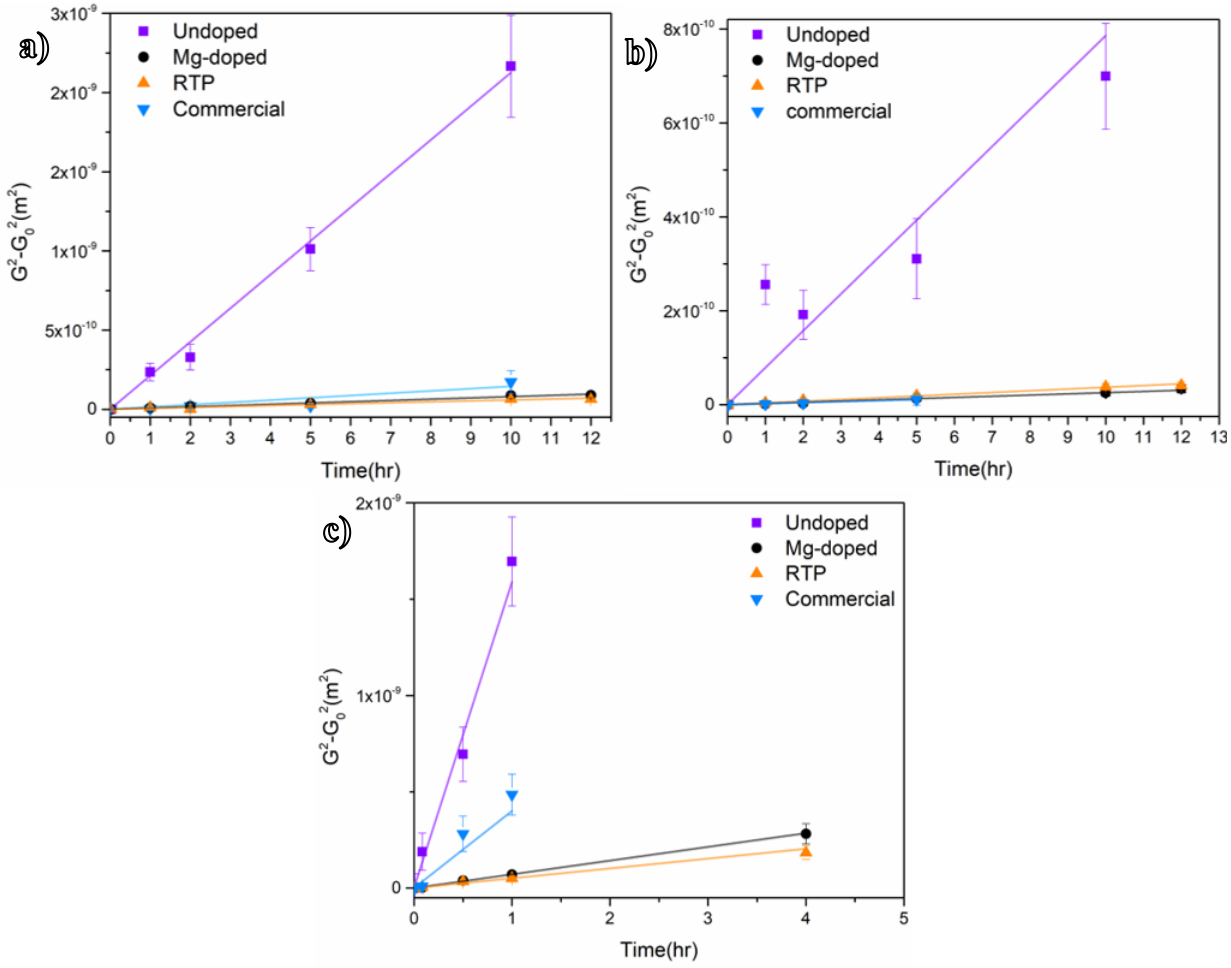

Figure 31: Grain growth kinetics of undoped, Mg doped, RTP and commercial RTP alumina samples annealed for various times at 1600°C in a) an air furnace, b) a graphite furnace and c) a field assisted furnace.

4.2.2.1 Grain Growth of Commercial RTP Alumina 98%

Additional annealing experiments were conducted to observe the growth behavior of a sample with an increased amount of glass. A 98% alumina sample was annealed in an air furnace at 1600°C showing two distinct growth regimes, defined from the slopes of linear behavior in Figure 32 The intersection between the two growth regimes was estimated to be 3.9 h, but the average grain size of sample annealed for 3 h (black) was about the same as of the one annealed for 5 h. the effective mobility for the orange regime is $1.07 \cdot 10^{-15} \frac{m^2}{sec}$ and for the blue regime is $7.9 \cdot 10^{-15} \frac{m^2}{sec}$.

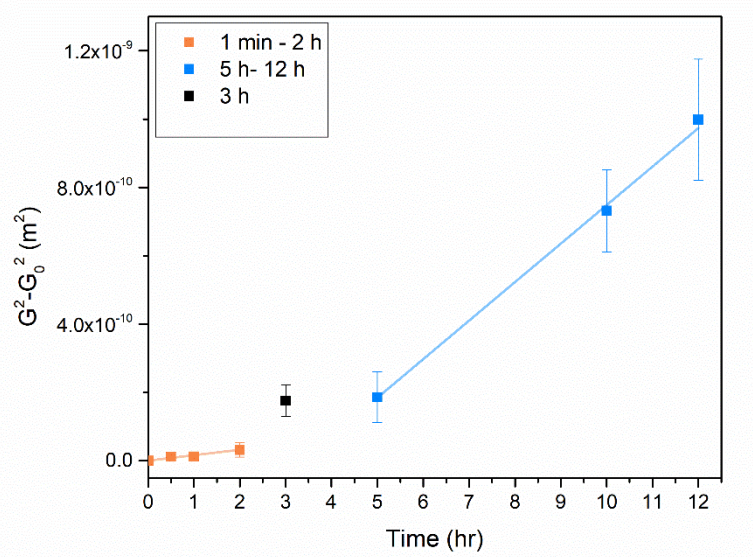

Figure 32: Grain growth kinetics of commercial RTP alumina 98% annealed for various times at 1600°C in an air furnace, exhibiting two growth regimes: initial (orange) and exaggerated (blue).

4.2.3 Grain Growth: Furnace Effect

The grain growth kinetics of four different samples, each after annealing treatments in the different furnaces, are presented in Figure 33. All samples annealed in the field assisted furnace showed significantly higher growth rates than those annealed conventionally in an air furnace, while those annealed in the graphite furnace showed lower growth rates.

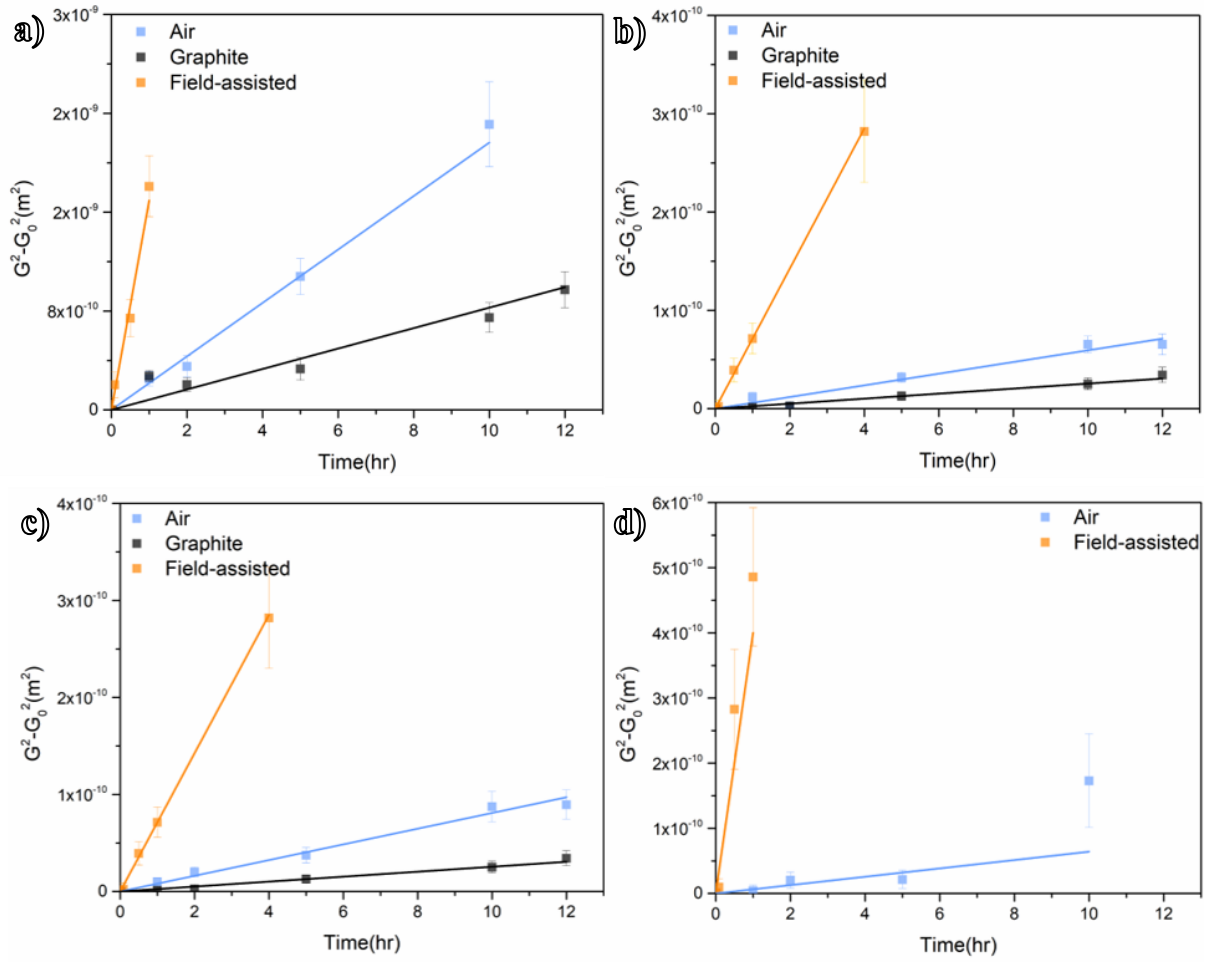

Figure 33: Grain growth kinetics of a) undoped, b) Mg doped, c) RTP and d) commercial RTP alumina samples, annealed at the different furnaces for various times at 1600°C.

4.2.4 Grain Boundary Mobility

The effective grain boundary mobility was determined from the parabolic grain growth kinetics and the results are presented in Table 4 and Figure 34. The results indicate different trends for various samples. Annealing samples in a field assisted furnace significantly increases the grain boundary mobility and annealing in a graphite furnace lowers the grain boundary mobility. For all furnaces, samples doped with Mg had in lower mobilities than the undoped ones.

Table 4: Summary of all measured grain boundary effective mobility values.

Sample	**Furnace**	**Effective mobility** $[\frac{m^2}{s}]$	**Error Values**$[\frac{m^2}{s}]$
Undoped	Field assisted furnace	$1.14 \cdot 10^{-13}$	$9.8 \cdot 10^{-15}$
Mg doped		$4.90 \cdot 10^{-15}$	$4.9 \cdot 10^{-17}$
RTP		$3.25 \cdot 10^{-15}$	$9.4 \cdot 10^{-17}$
Commercial RTP 99.5%		$3.48 \cdot 10^{-14}$	$2.7 \cdot 10^{-15}$
Undoped	Air furnace	$1.48 \cdot 10^{-14}$	$4.2 \cdot 10^{-15}$
Mg doped		$5.93 \cdot 10^{-16}$	$2.5 \cdot 10^{-17}$
RTP		$4.43 \cdot 10^{-16}$	$4.7 \cdot 10^{-17}$
Commercial RTP 99.5%		$1.01 \cdot 10^{-15}$	$2.7 \cdot 10^{-16}$
Commercial RTP 98%		$1.07 \cdot 10^{-15}$	$3.6 \cdot 10^{-17}$
Undoped	Graphite furnace	$5.10 \cdot 10^{-15}$	$4.9 \cdot 10^{-17}$
Mg doped		$1.86 \cdot 10^{-16}$	$1.0 \cdot 10^{-17}$
RTP		$2.55 \cdot 10^{-16}$	$5.1 \cdot 10^{-18}$
Commercial RTP 99.5%		$1.47 \cdot 10^{-16}$	$3.3 \cdot 10^{-17}$

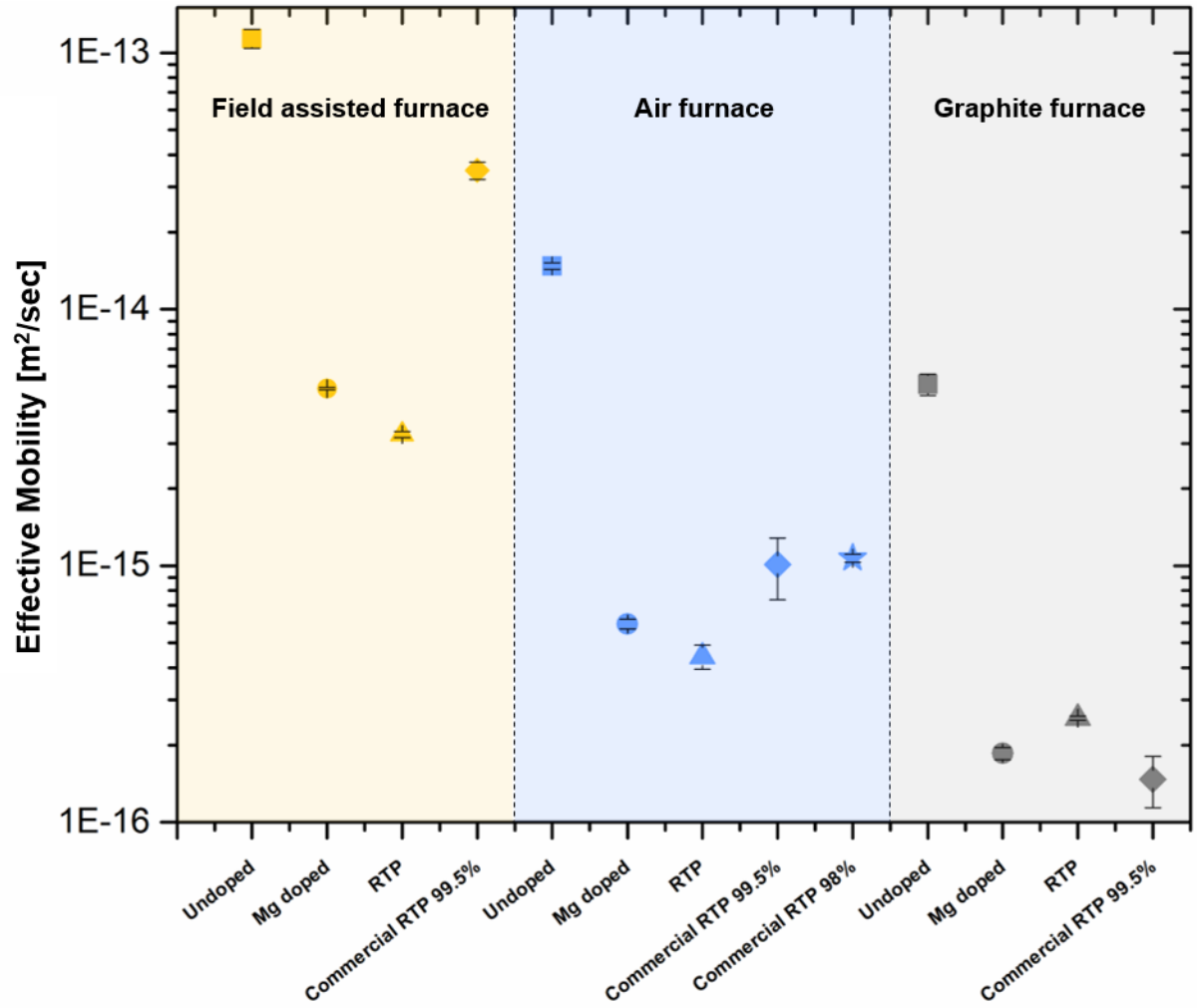

Figure 34: Effective mobilities presented in a graphical form (logarithmic scale)

4.3 Glass Exudation from Grain Boundaries

During sample preparation for SEM analysis, sample were cross sectioned, mechanically polished then thermally etched in air furnace at 1250°C for 2h, as described in section 3.3.6. After the thermal etch, a glassy phase was observed at most of the grain boundaries of the commercial RTP samples that contain 0.5% glass (Figure 35a), regardless of the furnace they were previously annealed in and the annealing time. This was not observed in samples containing dopants below the solubility limit (undoped, Mg doped and laboratory RTP). SEM EDS measurements done on the exuded phase indicated the presence of Ca, Si and in some areas Mg, meaning there had to be an excess of those dopants at the grain boundaries to be exuded as a glassy second phase.

New samples that underwent the same process but were thermally etched in a graphite furnace (under He flow) didn't exhibit any phase exuded from the grain boundaries. The same sample then underwent an additional thermal etch in an air furnace, then exhibited an exuded glassy second phase at the grain boundaries. To determine whether it is the low $P(O_2)$ of the carbon rich ambient in the graphite furnace that hinders exudation, an additional sample was polished and thermally etched in a sapphire tube furnace under Ar (low $P(O_2)$) at 1250°C for 2 h and demonstrated an exuded secondary phase.

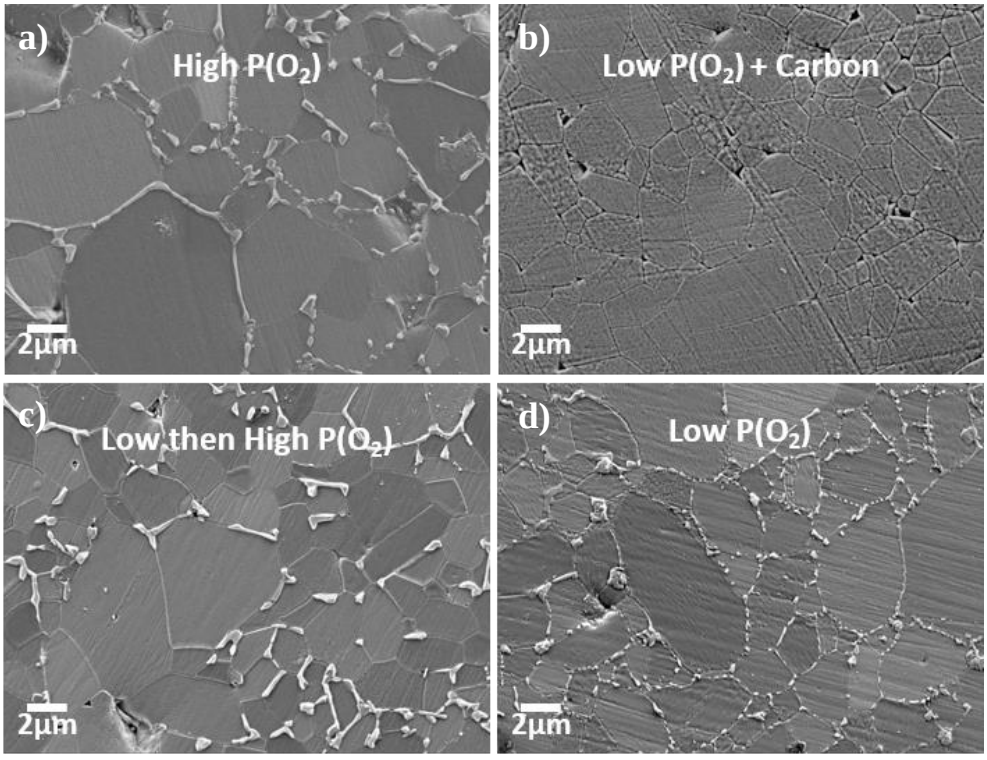

Figure 35: a) SE SEM micrograph of commercial RTP alumina sample thermally etched in an air furnace showing exuded glass at the grain boundaries. b) Thermally etched in a graphite furnace under flowing He showing no exuded phase at the grain boundaries. c) Sample b that underwent another thermal etch in an air furnace showing exuded glass at the grain boundaries. d) Thermally etched in a sapphire tube furnace under Ar showing exuded glass at the grain boundaries.

The dihedral angels θ_d of grain boundaries with and without an exuded glassy second phase were examined from a cross section of the samples that were etched in an air furnace and a graphite furnace respectively, using FIB. The dihedral angles of grooved grain boundaries after thermal etching in air and in a graphite furnace (Figure 36) were measured to be 74±3° and 98±2°, respectively. The contact angle between the exuded glass and alumina was measured to be $\theta_{Al_2O_3-glass} = 56°$ (Figure 36a, marked in blue).

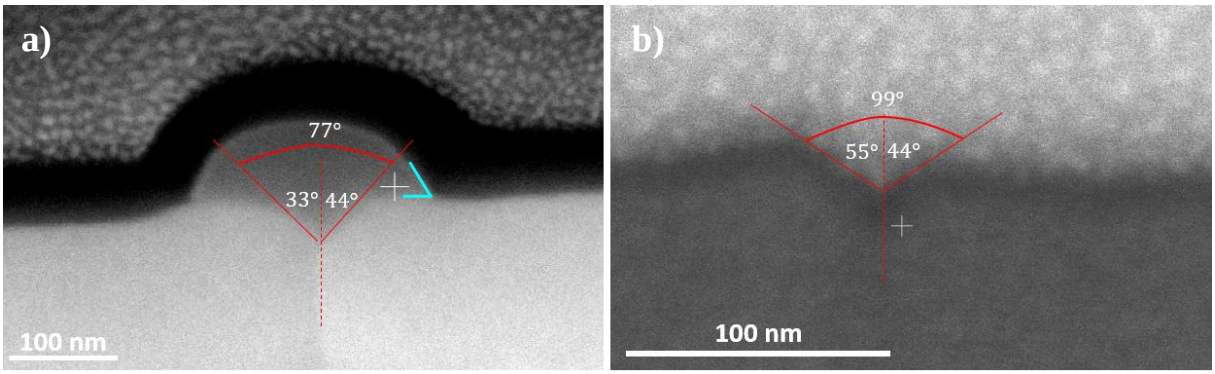

Figure 36: a) SE SEM micrograph of a sample (sectioned using the FIB) of a grain boundary cross-section in a sample annealed in air showing a glassy phase exuded from the boundary and partially wetting the grains. b) FIB micrograph of a grain boundary cross-section in a sample annealed in a graphite furnace under He.

A model wetting experiment was done with a sessile drop of soda-lime glass (SiO_2 doped with Na) on a sapphire wafer with the surface parallel to the basal plane for 2 h at 1250°C. This model was chosen to compare the wetting of the glass on sapphire after annealing in an air furnace and a graphite furnace (Figure 37), while avoiding different orientation of the polycrystalline alumina grains that have different surface and grain boundary energies. The contact angle of the sample annealed in an air furnace is $\theta^{air}_{Al_2O_3-glass} = 37 \pm 5°$. For the sample etched in a graphite furnace the angle couldn't be measured because of crystallization of the glass and collapse of the sessile drop (Figure 38).

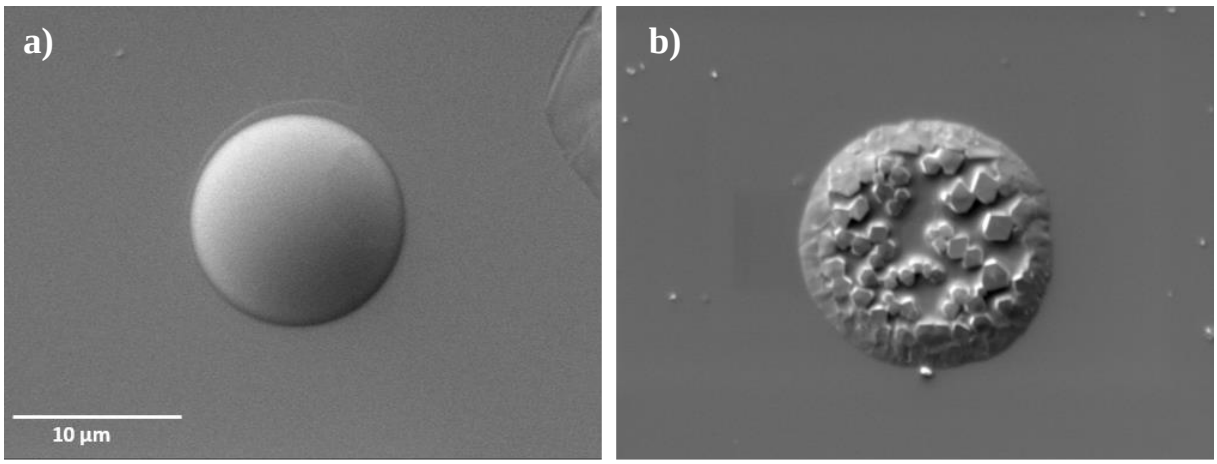

Figure 37: SE SEM micrograph of a soda-lime drop on a sapphire c-plane annealed for 2 h at 1250°C in: a) an air furnace, b) a graphite furnace (same scale bar for a and b).

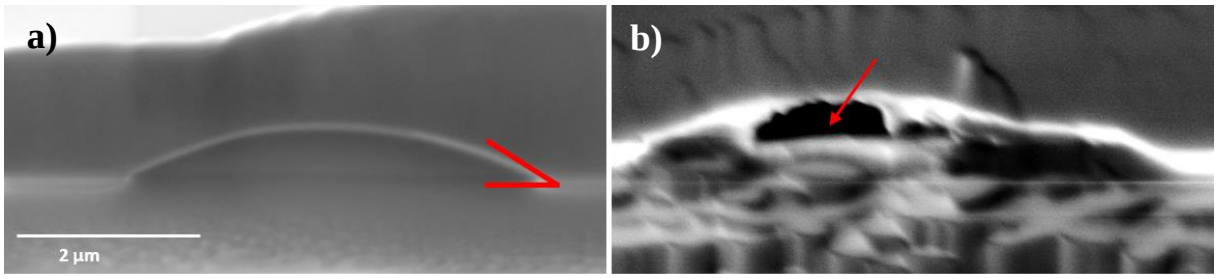

Figure 38: SE SEM micrograph of a sample (sectioned using the FIB) of (a) a drop cross-sectioned after annealing in an air furnace. The contact angle between the glass and the sapphire is marked in red. b) A collapsed drop of soda-lime glass on a sapphire c-plane surface annealed in a graphite furnace, where the void is marked with an arrow (same scale bar for a and b).

4.4 Wear Rate

Samples cut from the as sintered "mother samples" with varying compositions underwent wear rate experiment under the conditions mentioned in section 3.3.6.1. Table 5 summarizes all the samples properties:

Table 5: Summary of samples for wear rate experiment

Sample	Glass content [%]	Grain size [µm]	Density [%]
Laboratory RTP	0	4.8±1.6	99.6%
Commercial RTP 99.5%	0.5	4.5±3.8	99.3%
Commercial RTP 98%	2	4.4±2.7	98.8%

As can be seen in Figure 39, the wear rate is lower with the increase of glass content in the samples, meaning higher wear resistivity with increased glass content. Additional sample of commercial 90% alumina was prepared the same way as the 99.5% and the 98% alumina samples in order to check the wear rate with significant amount of glass in the sample, showing increased wear rate. Since the grain size of the sample wasn't fully analyzed, this increase might be due to larger grains or a change in adhesion at the grain boundaries due to the significant amount of glass present at the grain boundaries.

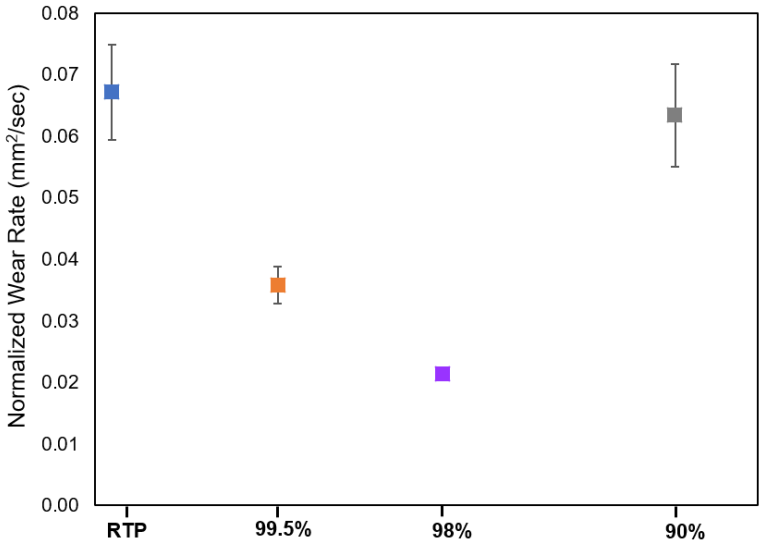

Figure 39: Wear rate of the different samples: laboratory RTP (blue), commercial RTP 99.5% (orange), commercial RTP 98% (purple) and commercial 90% (grey).

The bottom of the cutting groove was characterized by SEM for all samples (Figure 40) and shows that the fracture type changes from intergranular fracture for the laboratory RTP alumina sample to transgranular fracture for the commercial RTP 98% alumina sample. In addition, the formations of flat areas, which are so-called “tribofilms,” are visible in the three specimens. The tribofilm is known to form during the wear of alumina and is believed to be a layer of wear debris, however, its microstructure and composition are not fully understood [49]. They have a smooth surface and are expected to decrease the friction between diamond wafering blade and the alumina sample, increasing the apparent wear resistance [50]. In this experiment the surface covered by the tribofilm is very similar between the samples, so it is not expected to cause a significant difference between the samples.

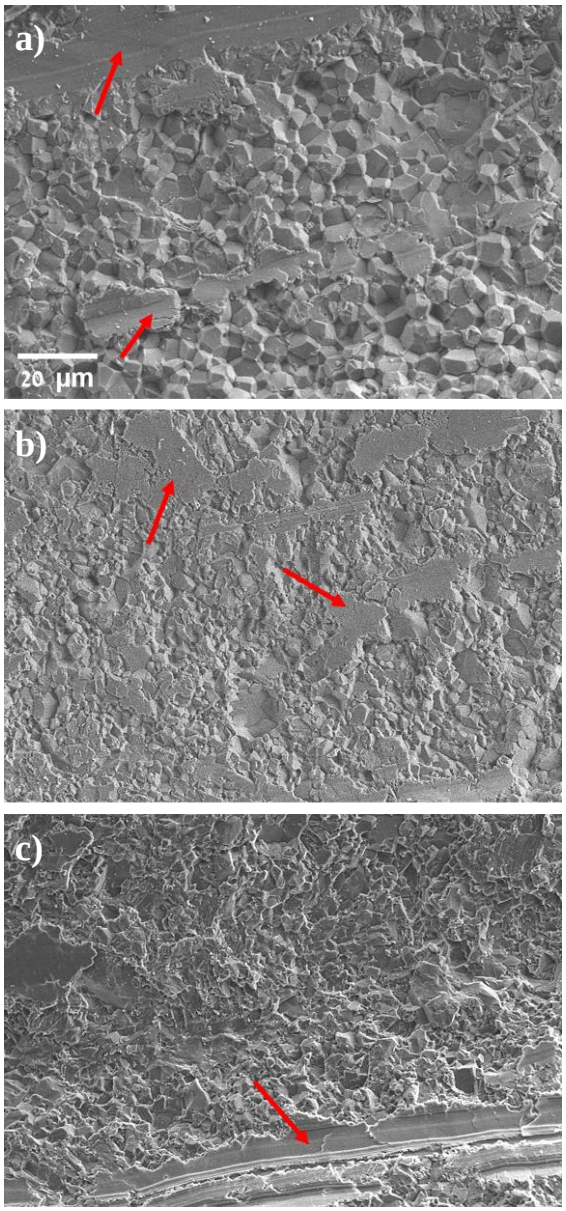

Figure 40: SE SEM micrographs of the wear surface for a) laboratory RTP alumina, b) commercial RTP 99.5% alumina and c) commercial RTP 98% alumina. Areas of tribofilm (marked in arrows) formed during cutting is shown in all samples. The micrographs show the bottom of a cutting groove, where abrasive wear by cutting took place (same scale bar for a, b and c).

Figure 41 presents a SE SEM micrograph of the bottom of a cutting groove in the 90% alumina sample showing large areas of tribofilm and large holes.

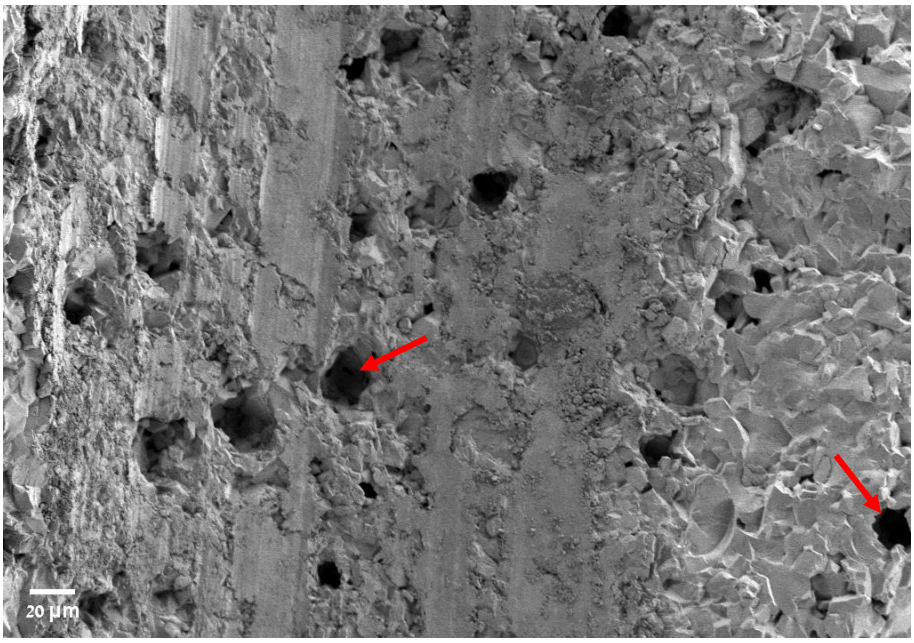

Figure 41: SE SEM micrograph of the wear surface for 90% alumina sample. The micrograph shows the bottom of a cutting groove, where abrasive wear by cutting took place. Visible pores with a diameter of the order of the diameter of abnormal grains are present at the surface of the groove and also at the fracture surface (marked in red arrows).

5. Discussion

5.1 The Influence of a Field on Grain Boundary Mobility

The effective mobility of undoped alumina annealed in a field assisted furnace is one order of magnitude higher than that of undoped alumina annealed in an air furnace and ~1.5 orders of magnitude higher than that of undoped alumina annealed in a graphite furnace. All the doped samples (Mg doped, laboratory RTP, commercial RTP alumina 99.5% and 98%) annealed in a field assisted furnace showed increased effective mobilities compared to the reduced mobilities for samples annealed in an air or a graphite furnace.

While studying the influence of electric fields during flash sintering of YSZ, Todd et al. correlated the rapid sintering (densification) rates mainly to rapid heating rates, rather than the influence from an electric field [51]. It was previously demonstrated in alumina and YSZ that the low voltages applied during FAST/SPS sintering did not have any observable difference compared to hot pressing, but densification did occur at lower temperatures in FAST sintering. Those experiments were done during the sintering process, where densification happened in parallel to grain growth and it is very hard to separate between the two phenomena [52,53]. This current work was done on fully dense samples, in order to separate between the densification process and grain growth. All the samples measured in this work started from a fully dense state, so any effect observed can be correlated to the applied field rather than to fast heating rates or densification starting at lower temperatures. Also, drag from pores is insignificant.

It was experimentally established in many works that field assisted sintering enables to reach fully dense samples in shorter times and lower temperatures, but there is still a debate on the way that the field affects grain growth, if it at all. There are studies that show reduced grain growth under an electric field [54,55], while others show enhanced grain growth and faster mobilities with an applied field [56,57,58,59,60]. It should be mentioned that reduction of grain growth was observed when during heating non-dense samples, and no evidence of grain growth inhibition was found for fully dense samples. It may be that the lack of quantitative measurements of mobility or the examination of non-dense samples in grain growth

experiments led to the conclusion that grain growth is slower under field assisted sintering. Also, different field strengths settings between different experiments have a different effect on the grain boundary mobility. Studies on fully dense samples mainly discuss grain growth and not grain boundary mobility. In this study the effective mobility of alumina grain boundaries under a field was measured, and it is a quantitative value that can be used to for comparison with different systems (doped alumina and even other materials). The results presented in Table 4 clearly show faster mobilities under a field.

Rheinheimer et al. studied the grain growth of a single crystalline $SrTiO_3$ seed diffusion-bonded to a *dense* polycrystalline matrix of strontium titanate using the FLASH sintering technique, Al_2O_3 insulators to ensure there is no current flow through the sample and joule heating. The electric field was found to induce higher grain growth rates, where a gradient of the growth rate of the single crystal between the two electrodes with grain growth being faster at the negative electrode. A point defect redistribution was presumed yielding a higher oxygen vacancy concentration near the negative electrode [56]. It was calculated that oxygen vacancies will segregate to interfaces due to the fact that their standard chemical potential is lower at the interface than in the bulk phase $\Delta\mu^{\Theta}_{|V_O|} < 0$ [61]. Since $SrTiO_3$ is a wide-bandgap semiconductor, a separation of the charged defect between the anodes could happen under the electric field. Even at the high temperatures (~1400°C-1500°C) at which the experiments were conducted, $SrTiO_3$ is few orders of magnitude more conductive than Al_2O_3 (in the range of 0.5 $\frac{1}{ohm \cdot cm}$ for $SrTiO_3$ and 10^{-7}-$6 \cdot 10^{-5}$ $\frac{1}{ohm \cdot cm}$ for Al_2O_3) [62,63], so alumina is more insulating. Also, Rheinheimer used DC electric fields while in the current study an AC electric field was used, so there is less potential for polarization in the alumina sample and the formation of charged defect gradients, because an AC field does not support permanent polarization as the direction of the field reverses every half cycle. This is probably why there is no grain growth gradient observed along the sample in this work, but there is an observed influence of electric fields on grain boundary mobility in both semi-conducting and non-conducting ceramics. The influence in this case is possible because the grain boundary itself is a charged defect. The observed increased in mobility is possible only if the disconnections move to one direction and don't move backward when the field alternates.

Gabay et al. also showed an increased grain boundary in SiC, which is a wide-bandgap semiconductor as well [60]. Conventional annealing in a graphite furnace of SiC resulted in a

grain boundary mobility of $3.53 \cdot 10^{-17} \frac{m^2}{sec}$, while SPS annealing resulted in a grain boundary mobility of $1.36\text{-}4.79 \cdot 10^{-14} \frac{m^2}{sec}$, which is a three orders of magnitude increase [60]. The lower increase shown in this current work between field assisted annealing and annealing in a graphite furnace might be attributed to the fact that Al_2O_3 is an insulator and might be influenced differently by the electric field. Moreover, the SiC was annealed at 2100°C while the Al_2O_3 was annealed at 1600°C, so different mechanisms activated by temperature or just faster kinetics might cause the difference.

Faster densification under an electric field is mostly agreed upon in the literature [54,64], while the exact mechanism for grain growth under a field is still unknown. The electric field might enable complexion transitions which may enhance the grain boundary mobility [35,65], create point defects such as oxygen vacancies or others [56] or even effect the dislocation motion of the grain boundaries, enhance the kinetic motion of disconnections and/or activate additional disconnection systems that may be cumulative, resulting in increased grain boundary mobility [12]. Further and deeper understanding of the mechanism of grain growth mobility will shed light of its behavior under an electric field.

5.2 The influence of carbon on Grain Boundary Mobility

Field assisted sintering is usually done using graphite crucibles that might introduce carbon to the samples. Samples from all the compositions were annealed in a graphite crucible to study its influence on the grain boundary mobility. All the samples annealed in the graphite furnace exhibit significantly lower mobilities than corresponding samples annealed in an air furnace or in a field assisted furnace.

Cohen et al. measured the solubility limit of of carbon in alumina at 1600°C to be 0.53 at.%, which is much higher than the solubility of other common dopants in alumina. They also demonstrated an increased solubility of Mg in a Mg-carbon co-doped alumina sample at 1600°C [66]. As the Mg concentration in the bulk increases, so does its availability for Gibbsian segregation to the grain boundaries and its influence on solute-drag. Cohen et al. also demonstrated that carbon from the sintering atmosphere can dissolve in alumina, where undoped (99.99%) alumina which was sintered in a graphite furnace resulted in a carbon

concentration of 607 ppm. The samples in this study that were annealed in the graphite furnace were dense, yet exhibited the change in color that is typical for carbon dissolution in the sample. This means that even dense samples annealed in the graphite furnace are doped with a certain amount of carbon. As for possible defects that might have formed in the low $p(O_2)$ and cause the color change, according to calculations done by Futazuka et al. the amount of point defects in pristine alumina is negligible in both low and high $p(O_2)$ [67].

Carbon segregation to grain boundaries in alumina was experimentally confirmed by Todd et al. using atom probe tomography [68]. Carbon adsorption to alumina grain boundaries results in solute-drag as an active mechanism, resulting in a finer microstructure, as shown by Marder et al. [69]. Therefore, even low carbon concentrations, including due to the use of graphite furnaces, can reduce grain growth of alumina. As mentioned, field assisted furnaces often use graphite crucibles, and the carbon from them can reduce the grain boundary mobility. However, from the results in this study we conclude that the influence of carbon is weaker than the influence of the electrical field.

It is still unclear why the effective mobility of Mg doped alumina sample is lower than the RTP that have higher Mg in the sample and also Mg spinel particles that inflict Zener drag. It is possible that there is a high solubility limit of carbon in spinel that takes away carbon from the grain boundaries.

5.3 The Influence of Liquid Phase on Grain Boundary Mobility

5.3.1 Undoped Sample

The mobility of undoped alumina sample sintered and annealed in air is compared with the mobility of other undoped alumina samples presented in the literature in Figure 42.

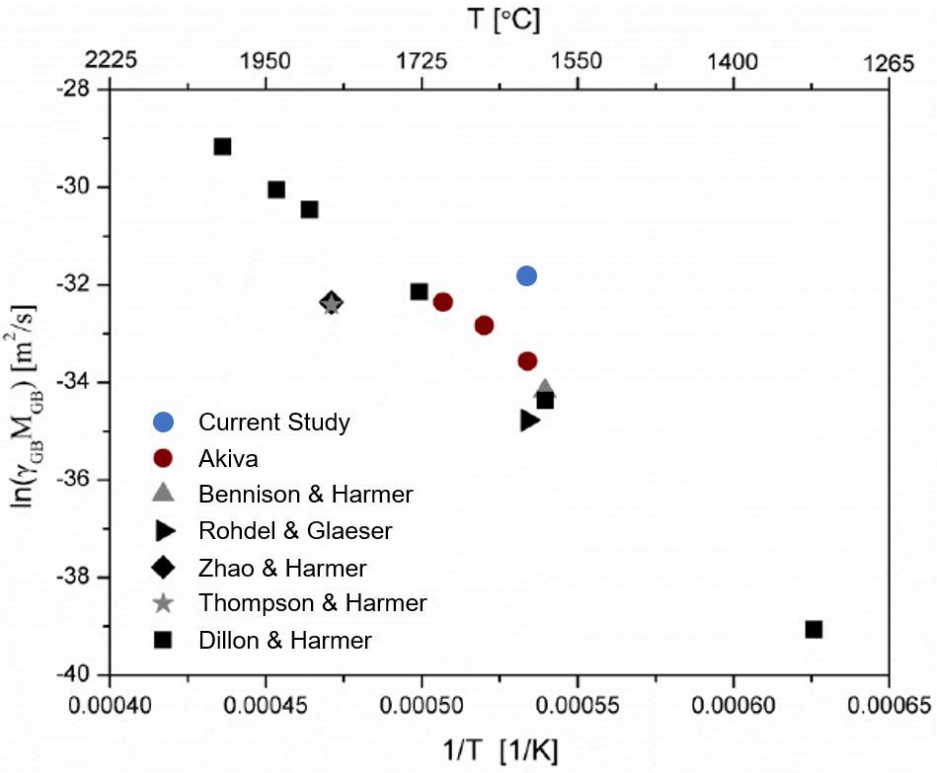

Figure 42: Effective grain boundary mobility for undoped alumina annealed in an air furnace, compared to effective mobility values from the literature. Redrawn from the data in [65].

The raw data from each published study was taken for samples above 97% density to ensure residual pores do not affect the grain boundary mobility (by Zener drag). The effective grain boundary mobility for the undoped alumina is higher compared to the existing literature [32,65,70,71,72,73]. Table 2 presents the dopant concentration in the undoped alumina sample, where the concentration of Si is about 50 ppm, below the solubility limit of Si in alumina at 1600°C but higher than the concentration stated by the manufacturer of ~15 ppm. Since Si is known as a grain boundary accelerator, Si adsorption might be the explanation for the higher effective mobility of the undoped alumina in this study.

Because all undoped samples made during this study are from the same batch, they can be compared one to the other. Despite the small amount of Si present in the samples, the trends in the mobility such as published in the literature are preserved. It should be noted that the values presented by Akiva [65] were recalculated from data in the literature using the parabolic law, although the data was originally obtained by other methods (such as the cubic form of equation (5)). Also, the dopants levels in the samples were not determined in the studies mentioned in the literature. All this might affect the effective mobility results, therefore one should be careful and critical when comparing the results between the different studies.

5.3.2 Samples with a Liquid Phase

The samples containing a liquid phase, commercial RTP 99.5% alumina and 98% alumina, have lower effective mobilities than undoped alumina samples in all furnaces. It should be noted that for the 98% alumina sample the growth rate changes after about 3 hours of annealing, which probably correlates to a change in the grain growth mechanism. For shorter annealing times the effective mobility of the 99.5% alumina and 98% alumina samples is about the same and as annealing time increases above 3 h for the 98%, the mobility increases significantly, yet still lower than undoped alumina.

The generalized form of equation (4) is:

$$\bar{G}_t^n - \overline{G_{t=0}}^n = kt \qquad (18)$$

In various systems, grain growth data follows different power laws. In a system of an impure single phase solute, if n is between 1 to 3, migration can be defined as being controlled by solution of a second phase n=1, a pure system or impurity drag at low solute content n=2, or impurity drag at high solute content n=3. For n=3 the kinetics might also fit to diffusion through a continuous second phase [74]. In the current study the best fit was for parabolic behavior with n=2 for grain growth in the polycrystalline samples in all compositions and furnaces. In most of other studies the grain growth was calculated according to the cubic law with n=3.

Blendell et al. [75] observed a decrease in grain growth rate of alumina samples containing liquid anorthite compared to undoped alumina samples. A further decrease in grain growth was observed when Mg was introduced to the system. Samples doped with Mg but without anorthite showed even slower grain growth rates. All samples were sintered at 1800°C by hot pressing at 35MPa under Ar or vacuum, inside a graphite die. These samples were compared to additional samples made by Spissler [76] that were prepared the same way as Blendell's samples but annealed at 1600°C and 1700°C. Bennison et al. annealed dense samples (sintered via hot pressing under vacuum) at 1600°C under flowing N_2 and also observed a slight decrease in grain boundary mobility when a certain amount of unintentional liquid phase was present, but a slight increase when comparing Mg-doped alumina with a certain amount of liquid phase [31,70]. Compared to the same experiment without a liquid phase where Mg decreases the grain

growth rate by a factor of 50 compared with undoped alumina, the combined liquid phase and Mg dropped it only by a factor of 5. Different methods were used in past studies to calculate the k ratio, which makes it difficult to compare between them.

Figure 43 summarizes the values (literature) of the grain growth constant, k, of alumina containing different amounts of glass with the k ratio of commercial RTP 99.5% and 98% samples.

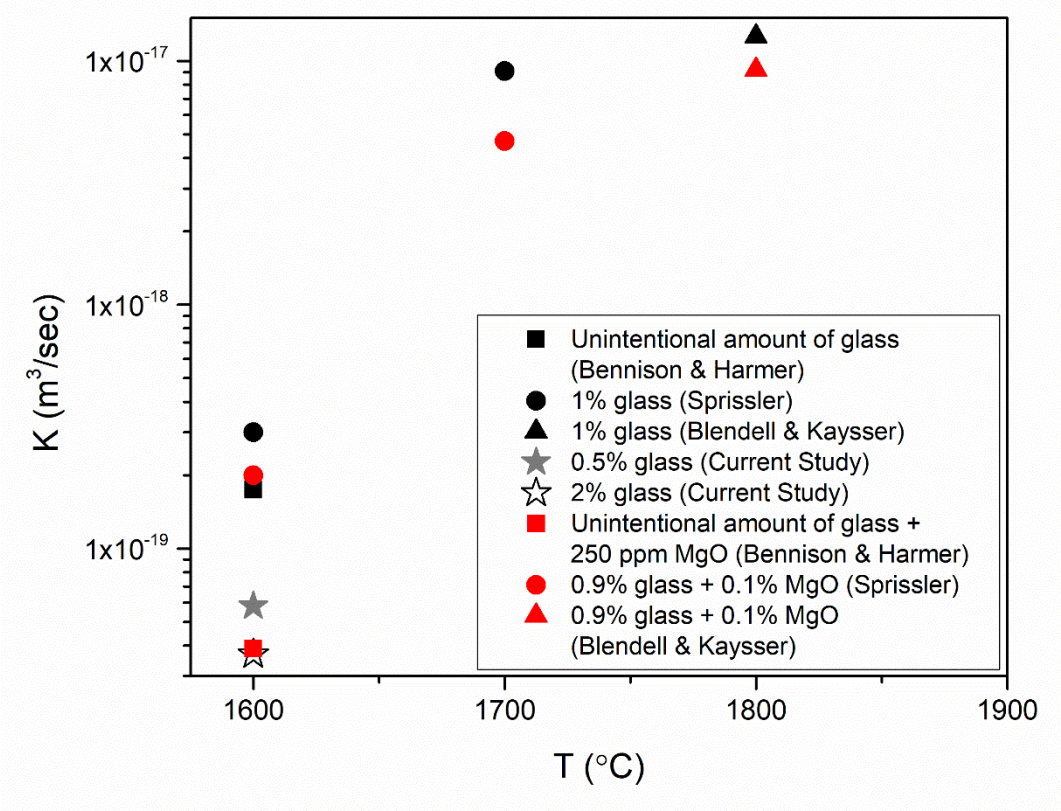

Figure 43: k ratio of commercial RTP 99.5% and 98% alumina compared with k ratio values from the literature for samples with varying amount of glass. Samples that contained only glass are marked in black, samples with additional doping of MgO marked in red. The commercial RTP samples in this current study contain Mg above solubility limit.

In order to compare the k ratio values for the samples studied here with data from the literature, the values were recalculated according to the cubic law (n=3). There was a poor fit of the present results to the cubic law and as a result a difference between the k values for the commercial RTP 99.5% and 98% alumina samples, while when calculated using the parabolic law their values were nearly identical.

The number of works that studied the mobility of alumina grain boundaries with a liquid phase is limited, and there are even less studies on dense samples, meaning that in the majority of the studies grain growth was measured with densification occurring at the same time. In each study the amount of glass added to the alumina was different and the final amount of glass in the sample after sintering was not measured. If the value of n is any indication for the amount of glass (n=2 correlates to impurity drag at low solute content and n=3 to high solute content) then according to the fitting analysis conducted in this study, the amount of glass in the alumina sample should be lower than the other studies where n=3. Also, the composition of the glass might vary between different studies, since according to the ternary phase diagram there is a range of compositions of SiO_2, CaO and Al_2O_3 with various solubility limits of additional dopants in the glass that might form in the sample [77,78]. Moreover, the different sintering and annealing techniques and ambient might introduce different dopants to the systems that might influence the measured results.

It can be seen in Figure 43 that the values of the k ratio of samples in this study which were doped with Mg above the solubility limit, are similar to those obtained by Bennison et al. in their MgO doped samples with small amount of liquid phase. Since the doping levels and annealing techniques are not similar it is hard to deduce a certain trend about the mobility with a liquid phase present, but it is certain to say that for all samples containing a liquid phase the addition of Mg decreases the grain growth k ratio, hence the effective mobility.

In studies done in the past [70,75] as well as this current study, samples with a liquid phase have lower mobilities than those of undoped alumina samples. Also, in this current study, commercial RTP 99.5% and 98% (in both grain growth regimes, see Figure 32) have lower effective mobilities than that of undoped alumina (Figure 34). This suggests that there is a rate limiting stage for grain growth, such as the dissolution and/or precipitation of atoms moving across the liquid phase. It is important to note that the effective mobility of alumina measured in this study might be higher due to the presence of Si in solution. If the effective mobility of the commercial RTP alumina measured in this study is compared with the undoped alumina from Akiva's study [65], the second grain growth regime in the 98% alumina have a higher effective mobility ($2.65 \cdot 10^{-15} \frac{m^2}{sec}$ compared to $7.9 \cdot 10^{-15} \frac{m^2}{sec}$ of the 98% alumina second regime). This might suggest that there is a limit of the liquid phase content or coverage where the liquid phase stops pinning the grain boundaries and start to accelerate the grain boundary mobility.

5.3.3 Glass Coverage

The glass coverage on the grain boundaries of alumina was calculated for 0.5% and 2% glass content, for three possible layer thicknesses, under the assumption of 1 gr of material with spherical grains and 99% density (Figure 44). 1µm layer thickness was chosen to resemble a bulk phase present at grain boundaries, 2 nm layer was chosen to resemble an adsorbed layer of solute and 50 nm was chosen according to Figure 20, where the average thickness of the glass layer present at the grain boundary was about 50 nm.

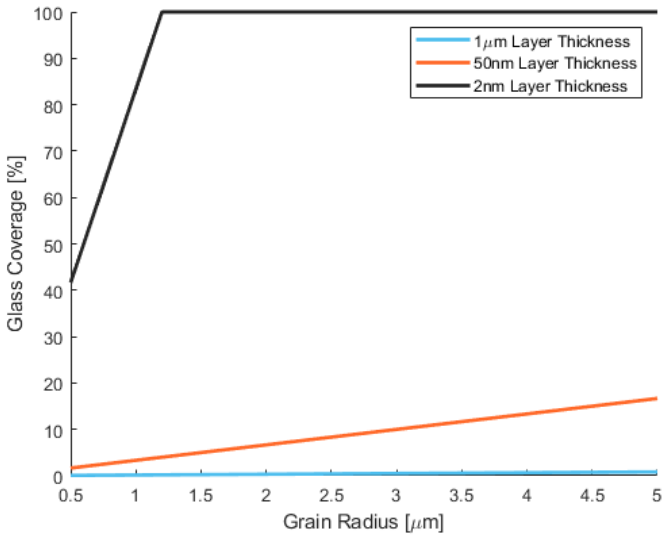

Figure 44: Glass coverage calculated for commercial RTP 99.5% alumina for three thickness layers: 1µm, 50 nm and 2 nm.

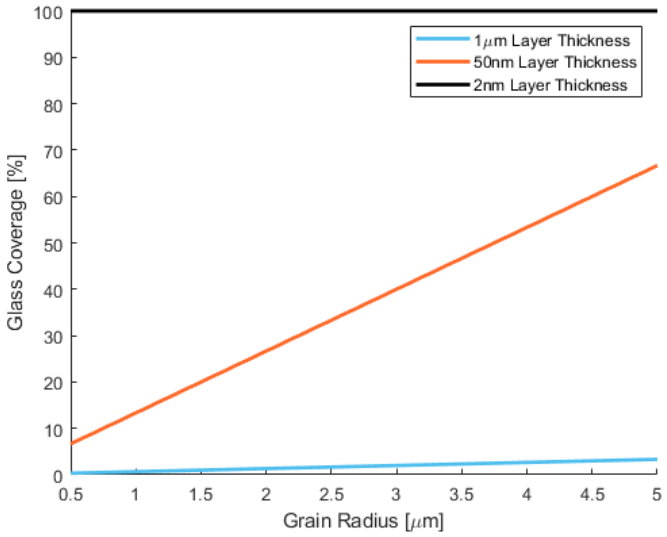

Figure 45:Glass coverage calculated for commercial RTP 98% alumina for three thickness layers: 1µm, 50nm and 2 nm.

According to the coverage calculation, a sample with a grain radius of 2 µm, which correlates to grain size of 4 µm which is about the initial grain size of the samples studied here, will be fully covered with an adsorbate layer from the beginning of the annealing experiment for both glass contents. If a glass layer of 50 nm thickness is considered, for a grain radius of 2 µm the coverage will be 5 times more for 2% glass compared with 0.5%. For both samples in the beginning of the annealing experiment most of the grain boundaries are not covered by glass. As grains grow, there is less grain boundary area to cover so the coverage increases. The different coverage change rate between 0.5% and 2% of glass might explain why in the commercial RTP 99.5% alumina there is only one grain growth regime while in the commercial RTP 98% alumina there is a change in the slope. After 3-4 hr of annealing, the grain radius in the commercial RTP 98% is about 7 µm which according to Figure 45 means that almost all the grain boundaries are covered with glass compared to much lower coverage when there is only 0.5% glass. There might be a glass coverage value at which the grain growth regime changes from interface control to diffusion through the liquid. The effective mobility of the second regime in the commercial RTP 98% alumina sample is faster than the first one by a factor of 7 which suggests that diffusion controlled grain boundary movement is faster. The phenomena seen in Figure 29 where there is a depletion of material between the thermally annealed grain boundaries of alumina where glass was shown to be present before thermal etching (Figure 27), might be explained by glass coverage. With shorter annealing times, the average grain size is smaller, hence larger grain boundary area, so there is a thinner layer of glass that evaporates during the thermal etching. With longer annealing times the average grain

size increases, the glass layer at grain boundaries is thicker so some of the glass still stays at the grain boundaries ass can be seen in Figure 29c.

Flaitz et al. studied the penetration of $CaO\text{-}SiO_2\text{-}Al_2O_3$ glasses into dense alumina samples [79]. They showed two stages of penetration, where the initial penetration was along triple junctions followed by penetration to grain boundaries by a solution/reaction between the liquid and alumina grain boundaries and interfaces and resulted in prismatic grains separated by glass. They also observed that doping the alumina with MgO decreases the penetration of the glass.

Hockey et al. studied sapphire bicrystal boundaries produced by liquid-phase sintering depended on the crystallographic misorientation of the crystals across the boundary and on the orientation of the boundary [80]. It was previously observed that prismatic low energy grain boundaries of alumina such as the c-plane (0001) and also $\{01\bar{1}2\}, \{10\bar{1}1\}, \{11\bar{2}0\}$ and $\{11\bar{2}3\}$ were wetted by the glass and faceted [81]. In Hockey's research they found that there is anisotropy of the glass wetting with different misorientation of the observed grain boundaries, meaning with different grain boundary energies. Dewetting of the glass occurred for low angle boundaries. In a previous research it was shown that roughly 84% of alumina grain boundaries were wetted by glass [82], but from Hockey's results it appears that grain boundary dewetting is more general than suggested in past studies. An example for dewetted grain boundary is shown in Figure 46, where alumina c-plane exhibits "pockets" of glass separated by dewetted regions containing adsorbed Si and Ca.

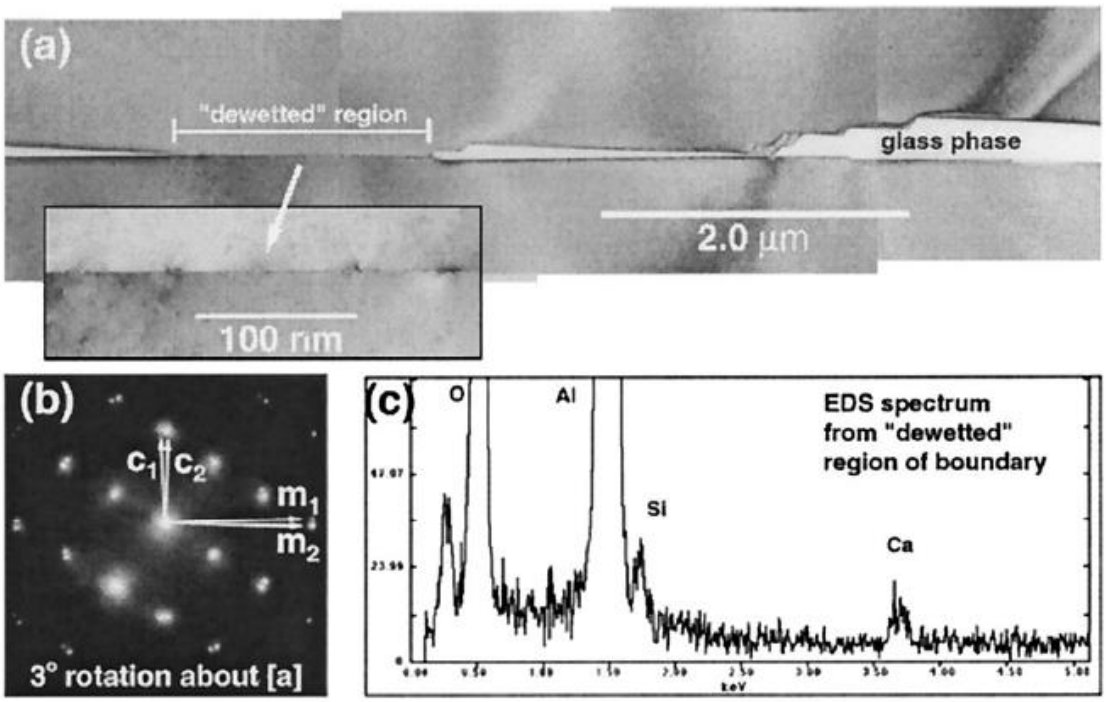

Figure 46: (a) Large-scale cross-sectional TEM view of a 3° basal tilt boundary viewed along the common a-axis of rotation. On this scale, the boundary is seen to consist of narrow, planar segments (designated as "dewetted") separated by interfacial glass pockets elongated along the boundary. (b) Selected area electron diffraction pattern confirming the 3° basal tilt misorientation. (c) Representative EDS spectrum from "dewetted" portion of boundary showing the presence of Si and Ca adsorbates at the boundary [80].

Flaitz's and Hockey's finding might explain the phenomena observed in this current research, where the commercial RTP 99.5% and 98% alumina samples have lower mobilities than the undoped alumina samples and with increased coverage the effective mobility increases.

As described in the first stage of glass penetration in Flaitz's study, with low coverage the glass might fill the triple junction first. The glass-filled triple junction pin the grain boundaries, hence decreasing their mobility. According to the suggested TLK model by Gleiter, the mechanism for grain boundary motion is by steps (disconnections- a defect with a step and/or grain boundary dislocation character) which likely form at triple junctions, where the process is diffusion of atoms to the grain surface which later attach to step sites and finally diffuse at the step to a kink site [12]. The fact that the grain boundaries have adsorbed glass-forming additives might affect the formation of the steps, hindering grain growth. When the coverage increases glass will anisotropically wet the grain boundaries themselves. Some grain boundaries will be dewetted as described in Figure 46, and the glass pockets present at the grain boundaries might pin the grain boundaries. When a significant layer of glass is present at the grain boundaries

(with increased coverage due to grain growth or increased glass content), there might be an influence on the disconnections motion with the increase of glass content at the grain boundaries. According to the solute-drag (or acceleration) theory, with increased solute in the material there is more influence on the mobility (marked in blue for drag and in red for acceleration in Figure 47 for a single grain boundary and in Figure 48 for multiple grain boundaries). Both of these trends discontinue near the solubility limit, where an abrupt decrease in mobility is expected due to a complexion transition at the grain boundaries. As described in Figure 47, the complexion transition occurs in a specific concentration of solute and as described decreases the mobility, probably due to a disturbance for disconnections motion. A complexion transition might also increase the mobility, if the complexion enables more disconnection motion. These trends might apply also to a liquid layer present at the grain boundaries, but further study on the behavior of disconnections at an interface between a grain and a liquid phase is needed.

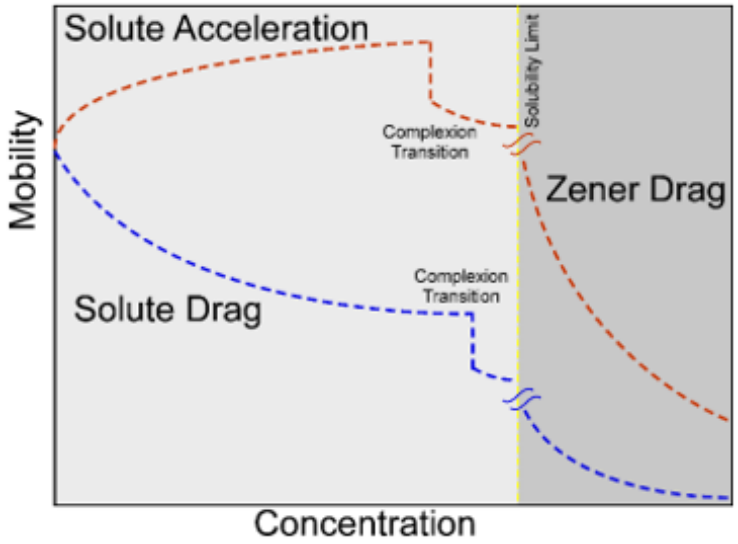

Figure 47: The hypothetical influence of composition on the mobility of a single grain boundary [83].

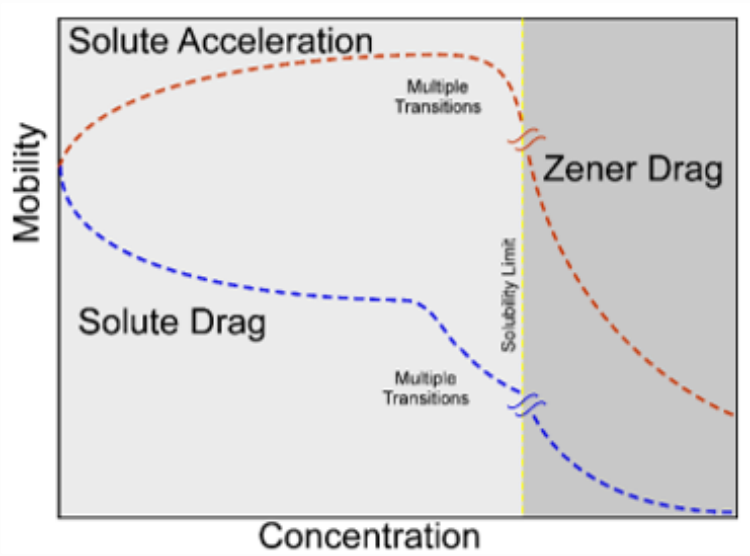

Figure 48: The hypothetical influence of composition on the mobility in a polycrystalline material [83].

Additional studies done on the behavior of glass wetted grain boundaries shown preferred wetting of alumina c-planes by the glass [75,84]. The wetted grain boundaries were reported to have slower mobilities than of "dry" grain boundaries, which raises the question whether the glass increases or decreases the effective grain boundary mobility? Is diffusion through the liquid indeed faster than grain growth by interface reaction or is the solution-precipitation of the atoms from the grain boundaries the rate limiting step? Since the grain growth mechanism, especially with liquid present, is not fully understood it is very hard to answer those questions.

The anisotropic wetting of the grain boundaries raises another question. Effective mobility is composed by two components as seen in equation (6); the grain boundary's energy and its mobility. Is it the lower energy of the wetted grain boundary that lowers the effective mobility?

Another aspect that needs to be considered is the Mg present in the commercial RTP alumina samples. It was shown in previous studies that Mg inflicts solute drag on alumina grain boundaries hence decreasing their effective mobilities [65]. Is it the Mg present in the glass that slows down the grain boundaries mobility? A study done by Chan et al. on the influence of high concentrations of liquid phase and MgO on the grain growth of alumina at 1600°C found that the liquid phase, compared with MgO, was the principal factor affecting the grain growth mechanism of alumina. Also, abnormal grain growth induced by anisotropic grain boundary wetting by glass was inhibited by MgO addition, but with increased glass amount and the same Mg amount the sample exhibited abnormal grain growth again. At 1600°C there is solubility of

Mg in the glass [85] so the liquid phase forming additives (Ca and Si) behaved as a scavenger for Mg and reduced the effect of Mg on the grain growth of alumina.

5.3.4 Wear Rate

For samples with about the same grain size and density the wear rate decreased with increased glass content, hence glass coverage. The microstructure of the cutting groove area observed by SEM exhibited a change of the nature of the fracture type with increased glass content, where it changes from intergranular fracture to transgranular. This might suggest that the grain boundaries become stronger with increased glass content, which is counterintuitive since the glass is brittle. A possible explanation is that tribofilms were formed from glass particles mixed with water during cutting and acted as a lubricant. With increased glass content there might be more lubrication during cutting.

The microstructure of the wear-groove in a 90% alumina sample observed by SEM revealed holes, with a diameter of the order of abnormal grains. Those holes might have formed due to grain pull-out during cutting. The observed holes are larger than the surrounding grains, which might suggest that coarser grains weakened the material, since it is known that the abrasive resistance of alumina deteriorates with larger grain size and boarder grain size distribution [86].

5.4 Exudation

The surface energies of (0001) sapphire and anorthite are 1.19 $\frac{J}{m^2}$ [87] and 0.483 $\frac{J}{m^2}$, respectively [88]. Baram et al. measured the anorthite-sapphire interface energy to be 0.743 $\frac{J}{m^2}$ [88]. Using Young's equation:

$$\gamma_{anorthite/Al_2O_3} = \gamma_{Al_2O_3} - \gamma_{anorthite} \cdot cos(\theta) \quad (19)$$

The contact angle between sapphire and anorthite should be $\theta_{anorthite/Al_2O_3} = 22°$, whereas in the presented system the measured contact angle of the glassy phase and polycrystalline alumina is 57±4 ° (Figure 36, marked in blue). The change in contact angle might be due to a change in the bulk chemistry compared to the studies of Baram et al., or due to adsorption of additional impurities to the surface(s) of the system. Also, there is a visible ridge, formed by

mass transport of alumina, between the glass droplet and the grain that might influence the force balance in the vertical direction and might cause a deviation in the measurement of the contact angle [89].

The dihedral angles of grooved grain boundaries after annealing in air and in a graphite furnace were measured to be 74±3 and 98±2 respectively. The interfaces energies were calculated accordingly, assuming isotropic surfaces and ignoring torque, where θ^* is the average of θ, ϕ:

$$\gamma_{GB} = 2\gamma_{solid-glass}^{avg} \cdot \cos(\theta^*) \rightarrow 2 \cdot cos(\theta^*) = \frac{\gamma_{GB}}{\gamma_{solid-glass}^{avg}} \quad (20)$$

Interface energy in air furnace: $2 \cdot \cos(37) = \frac{\gamma_{GB}}{\gamma_{s-glass}^{air}} = 1.7$

Interface energy in graphite furnace: $2 \cdot \cos(49) = \frac{\gamma_{GB}}{\gamma_{solid-vapor}^{\gamma_{He(CO/CO_2)}GB}} = 1.3$

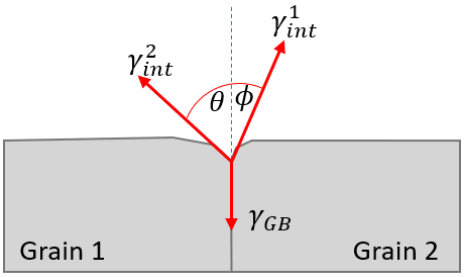

Figure 49: illustration of grain boundary with a grooved surface, showing the dihedral angles θ, ϕ and the interface energies γ_{int}.

In both cases the ratio is greater than 1, which means higher grain boundary energy compared to the surface/interface energy. It is known that for pure materials $\frac{\gamma_{GB}}{\gamma_S} \leq 1$. In the case of heat treatments in air, the new interface of exuded glass is energetically preferred rather than the free surface. Previous studies showed that carbon adsorbs to grain boundaries in alumina [90], and thus presumably also to the free surfaces of alumina. Therefore, carbon originating from the graphite furnace might reduce the alumina surface energy and reduce the driving force for glass exuding from grain boundaries to the surfaces of polished samples.

The contact angle of SiO_2 glass doped with Na (soda lime glass) and sapphire c-plane annealed in an air furnace and a graphite furnace was measured (Figure 38) in order to have a more accurate comparison without the effect of different grain boundary orientation with different

grain boundary energy. Alumina was previously demonstrated to change the temperature by which soda-lime glass crystallizes, however there was no consistent trend observed whether it is higher or lower between different soda-lima glass compositions [91]. The sample annealed in the graphite furnace exhibited solid crystals, meaning that the low $P(O_2)$ or carbon in the ambient might have changed the devitrification temperature of the glass, causing it to nucleate faster while glass annealed in air did not. Because of the crystals formed, the glass droplet was distorted and the contact angle between the glass and sapphire annealed in a graphite furnace could not be measured.

Since conventional surface characterization (e.g. XPS) will include carbon adsorbed during sample transfer from the furnace to the characterization tool, chemical analysis of carbon adsorption will require in situ experiments. In this study, annealing experiments were conducted in two annealing environments: an air furnace and a graphite furnace. In both cases, using the dihedral angles, the calculated ratio between the grain boundary and interface energies is larger than 1. In air furnace the new glass-alumina interface is assumed to have lower energy than free alumina surface. In the CO/CO_2 ambient in the graphite furnace, carbon might adsorb to the alumina surface and lower its energy.

6. Summary and Conclusions

Fully dense alumina with various compositions were annealed at 1600°C in three types of furnaces; an air furnace, a field assisted furnace, and a graphite furnace, in order to study the influence of electric fields and different doping below and above the solubility limit on the grain boundary mobility.

Mg in solution decreased the grain growth rate in samples annealed in all annealing atmospheres. The improved microstructure exhibited in various annealing ambients, together with increased surface diffusion shown elsewhere [92], indicates that additions of Mg is beneficial for both the densification and grain growth during sintering.

It was shown that a liquid phase containing Si and Ca above the solubility limit present during grain growth results in lower mobilities than of undoped alumina, but with increasing coverage of the grain boundaries by the liquid the mobility increases. Alumina samples doped below the solubility limit of Mg, Si and Ca exhibited even lower effective mobilities (due to solute drag of Mg and Zener drag by spinel perticles in the laboratory RTP samples), which emphasizes the importance of further understanding the mechanism of grain growth.

Annealing in a CO/CO_2 atmosphere decreases the mobility, most probably by carbon solute-drag.

For samples in all compositions an electrical field accelerated grain growth, yet the mechanism by which acceleration occurs is unknown. To the best of our knowledge this is the first time that accelerated grain boundary mobility under a field was demonstrated for an insulating material.

7. Recommendations for Future Work

This study used alumina with different doping as a case study for examining the influence of electrical field and a liquid phase on grain boundaries. By using dense samples, the separation between densification and grain growth was possible, and questions regarding the mechanism of grain growth in different conditions were raised.

The commercial powder used in this study contains significant amount of Mg. In order to further corroborate the decreased mobilities observed with a liquid phase present, additional grain growth experiments with increasing amounts of glass without Mg should be performed and analyzed.

The composition of glass might have an influence on the grain boundary mobility, so an experiment to determine the composition of the glass at grain boundaries and triple junctions should be conducted by quantitative STEM-EDS.

The behavior of disconnection motion is a key component in understanding grain growth behavior. In this research different effects of electric field and a liquid phase on the mobility of alumina grain boundaries were observed, so further analysis of dislocation motion under a field and when a liquid phase is present should be done. Also, quantitative measures of mobility for grain boundaries with a wetting film versus adsorbates at grain boundaries are lacking.

Increased mobilities with increased glass coverage were observed. The grain boundaries in the samples in this study were not fully wetted by glass at the beginning of the annealing experiments so additional set of measurements should be done on fully wetted samples.

Different behavior of the exudation of the glass during thermal annealing raised some questions. Does carbon change the composition of the glass? Does the composition of glass change with increased annealing times? Does carbon adsorb to alumina's surface and reduce the surface energy? To answer these questions a model wetting experiment of glass on a sapphire surface should be conducted in an air furnace and a graphite furnace with increased annealing times. The interface between the glass and the sapphire surface in the different furnaces should be characterized in terms pf orientation, structure and composition.

8. References

1. Kang, S. J. L. (2004). Sintering: densification, grain growth and microstructure. Elsevier.

2 Kingery, W. D., Bowen, H. K., & Uhlmann, D. R. (1976). Introduction to ceramics. John wiley & sons.

3 Coble, R. L. (1961). Sintering crystalline solids. I. Intermediate and final state diffusion models. Journal of applied physics, 32(5), 787-792.

4 Hong, S. H., & Kim, D. Y. (2001). Effect of liquid content on the abnormal grain growth of alumina. Journal of the American Ceramic Society, 84(7), 1597-1600.

5 German, R. M., Suri, P., & Park, S. J. (2009). Liquid phase sintering. Journal of materials science, 44(1), 1-39.

6 Carter, C. B., & Norton, M. G. (2007). Ceramic materials: science and engineering. New York: springer.

7 Bordia, R. K., Kang, S. J. L., & Olevsky, E. A. (2017). Current understanding and future research directions at the onset of the next century of sintering science and technology. Journal of the American Ceramic Society, 100(6), 2314-2352.

8 Groza, J. R. (2000). Field activation provides improved sintering. Metal Powder Report, 7(55), 16-18.

9 El-Mashad, H. M., & Pan, Z. (2017). Application of induction heating in food processing and cooking. Food Engineering Reviews, 9(2), 82-90.

10 M. N. Rahaman (2008), Sintering of Ceramics, second edition, CRC Press, Boca Raton, FL, USA.

11 R. Moshe, PhD research thesis, "The Influence of Dopants & Particles on the Kinetics of Microstructural Evolution of Alumina". Technion, Haifa, Israel (2019)

12 Gleiter, Herbert. "The mechanism of grain boundary migration." Acta Metallurgica 17.5 (1969): 565-573.

13 Hirth, J. P., & Pond, R. C. (1996). Steps, dislocations and disconnections as interface defects relating to structure and phase transformations. Acta materialia, 44(12), 4749-4763..

14 Sternlicht, H., Rheinheimer, W., Mehlmann, A., Rothschild, A., Hoffmann, M. J., & Kaplan, W. D. (2020). The mechanism of grain growth at general grain boundaries in SrTiO3. Scripta Materialia, 188, 206-211..

15 Newman, A., Krishnaprasad, P. S., Ponczak, S., & Brabant, P. (1998). Modeling and model reduction for control and optimization of epitaxial growth in a commercial rapid thermal chemical vapor deposition reactor.

16 Powers, J. D., & Glaeser, A. M. (1998). Grain boundary migration in ceramics. Interface Science, 6(1), 23-39.

17 M. N. Rahaman, Sintering of Ceramics, CRC Press, Boca Raton, FL, USA, p 580-582, 2008.

18 Cahn, J. W. (1962). The impurity-drag effect in grain boundary motion. Acta metallurgica, 10(9), 789-798.

19 Akiva, Ran, Alexander Katsman, and Wayne D. Kaplan. "Anisotropic grain boundary mobility in undoped and doped alumina." Journal of the American Ceramic Society 97.5 (2014): 1610-1618.

20 Dillon, S. J., & Harmer, M. P. (2007). Multiple grain boundary transitions in ceramics: a case study of alumina. Acta Materialia, 55(15), 5247-5254.

21 Zamir, Shlomit. "Si segregation and its role in reaching transparent YAG." Journal of the American Ceramic Society 100.4 (2017): 1689-1696.

22 Brook, R. J. "Pore-grain boundary interactions and grain growth." J. Am. Ceram. Soc. 52 (1969): 56-57.

23 Nicholson, G. C. "Grain growth in magnesium oxide containing a liquid phase." Journal of the American Ceramic Society 48.10 (1965): 525-528.

24 Lawrynowicz, D. E., J. Wolfenstine, and E. J. Lavernia. "Grain growth mechanisms in a spray-formed Ni3Al/Al2O3 composite in the presence of a liquid phase." Materials Science and Engineering: A 230.1-2 (1997): 1-13.

25 German, R. M., & Park, S. J. (2009). Handbook of mathematical relations in particulate materials processing: ceramics, powder metals, cermets, carbides, hard materials, and minerals. John Wiley & Sons.

26 Levin, Igor, and David Brandon. "Metastable alumina polymorphs: crystal structures and transition sequences." Journal of the american ceramic society 81.8 (1998): 1995-2012.

27 Kronberg, M. L. "Plastic deformation of single crystals of sapphire: basal slip and twinning." Acta Metallurgica 5.9 (1957): 507-524.

28 Brandon, David, and Wayne D. Kaplan. Microstructural characterization of materials. John Wiley & Sons, 2013

29 Coble, R. L. (1990). Sintering crystalline solids. II. Experimental test of diffusion models in powder compacts. In Sintering Key Papers (pp. 69-83). Springer, Dordrecht.

30 Berry, K. A., & Harmer, M. P. (1986). Effect of MgO solute on microstructure development in Al2O3. Journal of the American Ceramic Society, 69(2), 143-149.

31 Bennison, S. J., & Harmer, M. P. (1983). Effect of MgO solute on the kinetics of grain growth in A12O3. Journal of the American Ceramic Society, 66(5), C-90.

32 Rödel, J., & Glaeser, A. M. (1990). Anisotropy of grain growth in alumina. Journal of the American Ceramic Society, 73(11), 3292-3301.

33 Miller, L., Avishai, A., & Kaplan, W. D. (2006). Solubility limit of MgO in Al2O3 at 1600 C. Journal of the American Ceramic Society, 89(1), 350-353.

34 Akiva, R., Berner, A., & Kaplan, W. D. (2013). The solubility limit of CaO in α-alumina at 1600° C. Journal of the American Ceramic Society, 96(10), 3258-3264.

35 Dillon, S. J., & Harmer, M. P. (2008). Relating grain-boundary complexion to grain-boundary kinetics I: calcia-doped alumina. Journal of the American Ceramic Society, 91(7), 2304-2313.

36 Jung, J., & Baik, S. (2003). Abnormal grain growth of alumina: CaO effect. Journal of the American Ceramic Society, 86(4), 644-49.

37 Bae, I. J., & Baik, S. (1997). Abnormal grain growth of alumina. Journal of the American Ceramic Society, 80(5), 1149-1156.

38 Bae, S. I., & Baik, S. (1993). Sintering and grain growth of ultrapure alumina. Journal of materials science, 28(15), 4197-4204.
39 MacLaren, I., Cannon, R. M., Gülgün, M. A., Voytovych, R., Popescu-Pogrion, N., Scheu, C. & Rühle, M. (2003). Abnormal grain growth in alumina: synergistic effects of yttria and silica. Journal of the American Ceramic Society, 86(4), 650-59.
40 Dillon, S. J., & Harmer, M. P. (2008). Relating grain boundary complexion to grain boundary kinetics II: silica-doped alumina. Journal of the American Ceramic Society, 91(7), 2314-2320.
41 Park, C. W., & Yoon, D. Y. (2000). Effects of SiO2, CaO2, and MgO additions on the grain growth of alumina. Journal of the American ceramic society, 83(10), 2605-2609.
42 Lieberthal, Michael, and Wayne D. Kaplan. "Processing and properties of Al2O3 nanocomposites reinforced with sub-micron Ni and NiAl2O4." Materials Science and Engineering: A 302.1 (2001): 83-91.
43 Berg, J. C. (2010). An introduction to interfaces & colloids: the bridge to nanoscience. World Scientific.
44 Laidler, K. J., & McKenney, D. J. (1964). Kinetics and mechanisms of the pyrolysis of diethyl ether I. The uninhibited reaction. Proceedings of the Royal Society of London. Series A. Mathematical and Physical Sciences, 278(1375), 505-516.
45 Berner, A. I., Gimelfarb, F. A., & Ukhorskaya, T. A. (1982). Metrological aspects of micro-probe analysis. JOURNAL OF ANALYTICAL CHEMISTRY OF THE USSR, 37(2), 268-276.
46 Mendelson, M. I. (1969). Average grain size in polycrystalline ceramics. Journal of the American Ceramic society, 52(8), 443-446.
47 Moshe, R., Berner, A., & Kaplan, W. D. (2014). The Solubility Limit of SiO2 in α-alumina at 1600 C. Scripta Materialia, 86, 40-43.
48 Zaiou, S., Harabi, A., Harabi, E., Guechi, A., Karboua, N., Benhassine, M. T. & Guerfa, F. (2016). Sintering of anorthite based ceramics prepared from kaolin DD2 and calcite. Cerâmica, 62, 317-322.
49 Olofsson J, Jacobson S. The influence of grain size and surface treatment on the tribofilm formation on alumina components. Wear. 2012;292–293:17–24.
50 Chaiwan S, Hoffman M, Munroe P. Investigation of sliding wear surfaces in alumina using transmission electron microscopy. Sci Technol Adv Mater. 2006;7(8):826–33.
51 Ji, W., Parker, B., Falco, S., Zhang, J. Y., Fu, Z. Y., & Todd, R. I. (2017). Ultra-fast firing: Effect of heating rate on sintering of 3YSZ, with and without an electric field. Journal of the European Ceramic Society, 37(6), 2547-2551.
52 Langer, J., Hoffmann, M. J., & Guillon, O. (2009). Direct comparison between hot pressing and electric field-assisted sintering of submicron alumina. Acta Materialia, 57(18), 5454-5465.
53 Langer, J., Hoffmann, M. J., & Guillon, O. (2011). Electric field-assisted sintering in comparison with the hot pressing of yttria-stabilized zirconia. Journal of the American Ceramic Society, 94(1), 24-31.
54 Guillon, O., Gonzalez-Julian, J., Dargatz, B., Kessel, T., Schierning, G., Räthel, J., & Herrmann, M. (2014). Field-assisted sintering technology/spark plasma sintering: mechanisms, materials, and technology developments. Advanced Engineering Materials, 16(7), 830-849.
55 Conrad, H., & Wang, J. (2014). Equivalence of AC and DC electric field on retarding grain growth in yttria-stabilized zirconia. Scripta Materialia, 72, 33-34.

56 W. Rheinheimer, J. P. Parras, J.-H. Preusker, R. A. De Souza, and M. J. Hoffmann, Grain growth in strontium titanate in electric fields: The impact of space-charge on the grain-boundary mobility, Journal of the American Ceramic Society, 102[6] 3779-90 (2019).
57 W. Rheinheimer, X. L. Phuah, H. Wang, F. Lemke, M. J. Hoffmann, and H. Wang, The role of point defects and defect gradients in flash sintering of perovskite oxides, Acta Materialia, 165 398-408 (2019).
58 W. Qin, D. N. F. Muche, R. H. R. Castro, and K. van Benthem, The effect of electric fields on grain growth in MgAl2O4 spinel, Journal of the European Ceramic Society, 38[16] 5512-18 (2018).
59 L. A. Hughes, M. Marple, and K. van Benthem, Electrostatic fields control grain boundary structure in SrTiO3, Applied Physics Letters, 113[4] 041604-4 (2018).
60 Amir thesis
61 De Souza RA. The formation of equilibrium space-charge zones at grain boundaries in the perovskite oxide
SrTiO3. Phys Chem Chem Phys. 2009;11(43):9939–69.
62 Vollman M, Waser R. Grain boundary defect chemistry of acceptor-doped titanates: space charge layer width. J Am Ceram Soc.1994;77(1):235–43.
63 Florio JV. Dielectric properties of alumina at high temperatures. J Am Ceram Soc. 1960;43(5):262–7.
64 Becker, M. Z. E., Shomrat, N., & Tsur, Y. (2018). Recent advances in mechanism research and methods for electric-field-assisted sintering of ceramics. Advanced Materials, 30(41), 1706369.
65 R. Akiva, A. Katsman, and W.D. Kaplan, Anisotropic Grain Boundary Mobility in Undoped and Doped Alumina, Journal of the American Ceramic Society, 97[5]:1610-1618, 2014.
66 Cohen, L. O., Ghosh, P., Berner, A., Marder, R., & Kaplan, W. D. (2022). The Solubility Limit of Carbon in Alumina at 1,600 C. Microscopy and Microanalysis, 1-11.
67 Futazuka, T., Ishikawa, R., Shibata, N., & Ikuhara, Y. (2020). First-principles calculations of group IIA and group IV impurities in α− A l 2 O 3. Physical Review Materials, 4(7), 073602.
68 E. A. Marquis, N. A. Yahya, D. J. Larson, M. K. Miller, R. I. Todd (2010). Probing the improbable: imaging C atoms in alumina. Materials Today, 13(10), 34-36.
69 Marder, R., Ghosh, P., Reimanis, I., & Kaplan, W. D. (2021). The influence of carbon on the microstructure and wear resistance of alumina. Journal of the American Ceramic Society, 104(8), 4214-4225.
70 Bennison, S. J., & Harmer, M. P. (1985). Grain-Growth Kinetics for Alumina in the Absence of a Liquid Phase. Journal of the American Ceramic Society, 68(1), C-22.
71 J. Zhao and M. P. Harmer, _Effect of Pore Distribution on Microstructure Development: III, Model Experiments,‘ J. Am. Ceram. Soc., 75[4] 830-843 (1992).
72 A. M. Thompson and M. P. Harmer, Influence of Atmosphere on the Final-Stage Sintering Kinetics of Ultra-High-Purity Alumina,‘ J. Am. Ceram. Soc., 76[9] 2248-2256 (1993).
73 S. J. Dillon and M. P. Harmer, Intrinsic Grain Boundary Mobility in Alumina, ‘J. Am. Ceram. Soc., 89[12] 3885-3887 (2006).

74 R. J. Brook, Controlled Grain Growth, 'pp.331-364 in Treatise on Materials Science and Technology: Ceramic Fabrication Processes, Vol. 9 Edited by F. F.Y. Wang, Academic, NY, 1976.

75 Kaysser, W. A., Sprissler, M., Handwerker, C. A., & Blendell, J. E. (1987). Effect of a liquid phase on the morphology of grain growth in alumina. Journal of the American Ceramic Society, 70(5), 339-343.

76 M. Snrissler: Ph.D. Thesis. Universitv of Stutteart. Stutteart. I'cdcral Kcnuhlic 01- Germany, 1981.

77 DeVries, R. C., & Osborn, E. F. (1957). Phase Equilibria in High-Alumina Part of the System CaO–MgO–Al2O3–SiO2. Journal of the American Ceramic Society, 40(1), 6-15.

78 E. Haccuria, T. Crivits, P. C. Hayes, E. Jak (2016). Selected phase equilibria studies in the Al2O3–CaO–SiO2 system. Journal of the American Ceramic Society, 99(2), 691-704.

79 Flaitz, P. L., & Pask, J. A. (1987). Penetration of polycrystalline alumina by glass at high temperatures. Journal of the American Ceramic Society, 70(7), 449-455.

80 Hockey, B. J., Wiederhorn, S. M., Blendell, J. E., Lee, J. S., & Kang, M. K. (2003). Structure of Sapphire Bicrystal Boundaries Produced by Liquid-Phase Sintering. Journal of the American Ceramic Society, 86(4), 612-22.

81 Choi, J. H., Kim, D. Y., Hockey, B. J., Wiederhorn, S. M., Handwerker, C. A., Blendell, J. E., Roosen, A. R. (1997). Equilibrium shape of internal cavities in sapphire. Journal of the American Ceramic Society, 80(1), 62-68.

82 Shaw, T. M., & Duncombe, P. R. (1991). Forces between aluminum oxide grains in a silicate melt and their effect on grain boundary wetting. Journal of the American Ceramic Society, 74(10), 2495-2505.

83 R. Moshe, PhD thesis, "The Influence of Dopants & Particles on the Kinetics of Microstructural Evolution of Alumina", Technion,Haifa,Israel (2019)

84 Chan, T. Y., Liu, S. J., & Lin, S. T. (1998). Effects of high concentrations of liquid phase and magnesia on the grain growth of alumina. Ceramics international, 24(8), 617-625.

85 Kingery, W. D., Bowen, H. K., & Uhlmann, D. R. (1976). Introduction to ceramics (Vol. 17). John wiley & sons, 1976, p. 307.

86 Miranda-Martinez, M., Davidge, R. W., & Riley, F. L. (1994). Grain size effects on the wet erosive wear of high-purity polycrystalline alumina. Wear, 172(1), 41-48.

87 G. Levi, W. D. Kaplan (2003). Aluminium-alumina interface morphology and thermodynamics from dewetting experiments. Acta Materialia, 51(10), 2793-2802.

88 M. Baram, D. Chatain, W. D. Kaplan (2011). Nanometer-thick equilibrium films: the interface between thermodynamics and atomistics. Science, 332(6026), 206-209.

89 Saiz, E., A. P. Tomsia, and R. M. Cannon. "Ridging effects on wetting and spreading of liquids on solids." Acta Materialia 46.7 (1998): 2349-2361.

90 E. A. Marquis, N. A. Yahya, D. J. Larson, M. K. Miller, R. I. Todd (2010). Probing the improbable: imaging C atoms in alumina. Materials Today, 13(10), 34-36.

91 Morey, G. W. (1930). THE EFFECT OF ALUMINA ON THE DEVITRIFICATION OF A SODA-LIME-SILICA GLASS 1. Journal of the American Ceramic Society, 13(10), 718-723.

92 Bennison, S. J., & Harmer, M. P. (1990). Effect of Magnesia Solute on Surface Diffusion in Sapphire and the Role-of Magnesia in the Sintering of Alumina. Journal of the American Ceramic Society, 73(4), 833-837.